MOJAVE: Monitoring of jets in active galactic nuclei with VLBA experiments. I. First-epoch 15 GHz linear polarization images

M. L. Lister   D. C. Homan

MOJAVE: MONITORING OF JETS IN ACTIVE GALACTIC NUCLEI WITH VLBA EXPERIMENTS. I. FIRST-EPOCH 15 GHz LINEAR POLARIZATION IMAGES

M. L. LISTER

Department of Physics, Purdue University, 525 Northwestern Avenue, West Lafayette, IN 47907; mlister@physics.purdue.edu

AND

D. C. HOMAN

Department of Physics and Astronomy, Denison University, Granville, OH 43023; homand@denison.edu

ABSTRACT

We present first-epoch, milliarcsecond-scale linear polarization images at 15 GHz of 133 jets associated with active galactic nuclei (AGNs) from the MOJAVE (Monitoring of Jets in Active Galactic Nuclei with VLBA Experiments) survey. MOJAVE is a long-term observational program to study the structure and evolution of relativistic outflows in AGNs. The sample consists of all known AGNs with Galactic latitude $|b| > 2°.5$, J2000.0 declination greater than $-20°$, and correlated 15 GHz Very Long Baseline Array (VLBA) flux density exceeding 1.5 Jy (2 Jy for sources below the celestial equator) at any epoch during the period 1994–2003. Of the 133 AGNs that satisfy these criteria, 96 are also part of the VLBA 2 cm Survey. Because of strong selection effects, the sample is dominated by blazars with parsec-scale morphologies consisting of a bright core component at the extreme end of a one-sided jet. At least one-third of the cores are completely unresolved on the longest VLBA baselines, indicating brightness temperatures above 10^{11} K. These cores tend to have electric vectors that are better aligned with the inner jet direction, possibly indicating the presence of a stationary shock near the base of the jet. The linear polarization levels of the cores are generally low ($<5\%$), but many of the extended jet regions display exceedingly high fractional polarizations ($>50\%$) and electric vectors aligned with the jet ridge line, consistent with optically thin emission from transverse shocks. The cores and jets of the radio galaxies show very little or no linear polarization. Both the weak- and strong-lined blazar classes (BL Lac objects and high-polarization radio quasars) show a general increase in fractional polarization with distance down the jet, but the BL Lac jets are generally more polarized and have electric vectors preferentially aligned with the local jet direction. We show that these differences are intrinsic to the jets and not the result of observational biases. We find that distinct features in the jets of gamma-ray-loud (EGRET) blazars are typically twice as luminous as those in non-EGRET blazars and are more highly linearly polarized. These differences can be adequately explained if gamma-ray blazars have higher Doppler-boosting factors, as the result of better alignment with the line of sight and/or higher bulk Lorentz factors.

Key words: BL Lacertae objects: general — galaxies: active — galaxies: jets — polarization — quasars: general — radio continuum: galaxies

Online material: color figures, machine-readable tables

1. INTRODUCTION

In terms of total energy output, active galactic nuclei (AGNs) represent some of the most energetic phenomena known in the universe and provide unique laboratories for studying a variety of high-energy physical processes associated with special and general relativity, particle acceleration, and magnetohydrodynamics. Of particular interest are the roughly 10% of all AGNs that generate massive outflows that emit powerful broadband synchrotron and inverse Compton radiation. Direct imaging of the radio synchrotron emission from AGN outflows using the Very Long Baseline Array (VLBA) has revealed that the outflows are highly collimated, relativistic jets of material with apparent superluminal speeds up to $\sim40c$ (Jorstad et al. 2001b; Kellermann et al. 2004). Images on larger scales show that many are able to remain collimated for hundreds of kiloparsecs before depositing enormous energies ($\sim10^{61}$ ergs) into large plumes of radio-emitting plasma.

The highly relativistic speeds of AGN jets have a substantial impact on their observed properties, including their apparent speeds, variability timescales, viewing angles, and apparent luminosities. According to a stationary observer, the radiation from a relativistic bulk flow will be highly Doppler-boosted (i.e., beamed) in a forward direction. Any flux-limited sample selected on the basis of this jet emission will therefore preferentially contain jets viewed nearly end-on. For such an orientation, transverse speeds faster than light are possible, and early VLBI observations (e.g., Cohen et al. 1977) were able to detect these apparent superluminal motions in bright, discrete knots that moved outward at steady speeds from a stationary "core" that is assumed to be associated with an optically thick region near the base of the jet.

The NRAO's[1] VLBA has radically changed our view of AGN jets, making it possible to routinely obtain high dynamic range, full-polarization images at regular intervals. It is now evident that AGN jets are complex magnetohydrodynamic phenomena that cannot be adequately modeled using simple analytical methods or models involving purely ballistic "knots." They are best described as highly magnetized fluids that respond to changes in the conditions at their nozzles and in their external environments. The unsuitability of analytical models implies that computer simulations are essential for fully understanding

---

[1] The National Radio Astronomy Observatory is a facility of the National Science Foundation operated under cooperative agreement by Associated Universities, Inc.

the physics of jet phenomena. Indeed, there are many groups that are making important advances in this area (e.g., Hughes et al. 2002; Koide et al. 2002; Aloy et al. 2003). However, to be effectively applied, these simulations require a large set of observational constraints that are best provided by VLBI arrays, because of their high angular resolution and ability to penetrate through obscuring material in the host galaxies. Although numerous detailed VLBI studies have been made of nearby and unusual individual jets, so far there have been few large statistical studies to investigate the overall properties of the general jet population. In an earlier study using the Pearson-Readhead survey, we demonstrated the advantages in gathering a large amount of data on a small sample (Lister et al. 2001) by identifying several new observational correlations and providing conclusive evidence of relativistic beaming in blazars. However, little could be inferred about the general jet population because of the small sample size (32 objects) and the presence of complex selection biases. These biases can create artificial correlations in blazar samples and lead to incorrect conclusions. Fortunately, it is possible to properly account for these biases, given a complete sample that is sufficiently large ($\gtrsim 100$ jets), with rigorous selection criteria based on beamed jet emission (Lister & Marscher 1997).

In order to address these issues, we have begun a large, full-polarization VLBA campaign on a complete AGN sample with the goal of providing the best possible data set for investigating the statistical properties of AGN jets and modeling their selection biases. MOJAVE (Monitoring of Jets in Active Galactic Nuclei with VLBA Experiments) is a complement to the recent VLBA 2 cm Survey (Kellermann et al. 1998, 2004; Zensus et al. 2002). The latter program regularly imaged over 150 AGN jets from 1994 to 2002 and made significant discoveries regarding the general kinematics of AGN jets, including the finding that highly superluminal jets are extremely rare and that the observed pattern speeds are directly connected with the underlying flow. The 2 cm Survey did not, however, investigate the magnetic field evolution of jets, since its observations were of total intensity (Stokes I) only. Also, the survey was drawn from a low-frequency all-sky catalog and was statistically incomplete from the standpoint of beamed jet emission. As we describe in § 2.1, MOJAVE uses a complete sample selected on the basis of 15 GHz VLBA flux density only.

Although the 2 cm Survey contained the longest continuous monitoring baselines of any VLBI survey carried out to date, reliable speeds could only be measured in roughly 75% of the sources (Kellermann et al. 2004). In the remainder, the angular motions were either too slow (because of low intrinsic speed or high redshift of the host galaxy) or exhibited too few distinct features that could be tracked during the observation interval. Also, a small number of nearby sources displayed very fast motions that were undersampled by the monitoring intervals. The MOJAVE program is correcting these deficiencies by increasing the monitoring baseline for the slow sources by an additional 3 yr and sampling the faster sources more frequently. With our current program, we observe each source at intervals ranging from a few months to 1 yr. We will have obtained at least four additional epochs on each source by the end of our program. All of our calibrated data and images are available online at the MOJAVE program home page.[2]

As MOJAVE is the first multiepoch VLBI project to provide full linear and circular polarization information on a large sample of AGN jets, many of its goals are statistical in nature. Here we discuss the overall linear polarization characteristics of

our sample based on our first-epoch observations only. Details on unusual individual sources, as well as the overall evolution and circular polarization properties of the sample, will be presented in subsequent papers.

The overall layout is as follows. In § 2 we discuss the selection criteria and general properties of the MOJAVE sample. In § 3 we describe our observations and data reduction technique, as well as the general method for deriving observational quantities. We discuss the overall polarization characteristics of the sample in § 4 and describe distinct differences in the jets of BL Lac objects and quasars, as well as gamma-ray- and non-gamma-ray-detected blazars. We summarize our main conclusions in § 5.

We adopt a contemporary cosmology with $\Omega_m = 0.3$, $\Omega_\Lambda = 0.7$, and $H_0 = 70$ km s^{-1} Mpc^{-1}. Our position angles are given in degrees east of north, and all fractional polarization quantities refer to linear polarization only. We use the convention $S_\nu \propto \nu^\alpha$ for the spectral index.

2. THE MOJAVE SAMPLE

2.1. Selection Criteria

The goals of the MOJAVE program demand a statistically complete AGN jet sample that is bright enough for direct fringe detection with the VLBA and whose properties can be compared with theoretical models incorporating relativistic beaming effects (e.g., Lister & Marscher 1997). Samples selected via total (single-dish) radio flux density without regard to spectral index are not suitable, since they are dominated by radio galaxies with luminous, extended lobe structure. Their parsec-scale jets are very faint, and imaging them usually requires time-intensive VLBI phase-referencing techniques. Since their jets lie much closer to the plane of the sky than blazars, there is very little Doppler time compression, resulting in much slower evolution and often subluminal speeds. Also, simulating the observational biases in such a sample requires detailed knowledge of the relationship between intrinsic jet luminosity and extended lobe power, which is currently not well constrained.

An approach more suited to our goals involves constructing an AGN sample based on beamed jet emission only. By using the milliarcsecond scale (VLBA) 15 GHz flux density as a selection criterion, one can effectively exclude the contribution from large-scale emission, leaving a sample consisting almost entirely of radio-loud AGNs with relativistic jets pointed nearly directly at us (i.e., blazars). The only exceptions are a few nearby radio galaxies and several peaked-spectrum sources whose jet axes likely lie much closer to the plane of the sky.

The selection criteria we have chosen for the MOJAVE sample are similar to those of the VLBA 2 cm Survey and are summarized as follows:

1. J2000.0 declination $\geq -20°$.
2. Galactic latitude $|b| \geq 2°.5$.
3. Total 15 GHz VLBA flux density of at least 1.5 Jy (or 2 Jy for southern sources) *at any epoch* during the period 1994–2003.

Because of the variable nature of strong, compact AGNs, we have not limited the flux density criterion to a single fixed epoch. Doing so would have excluded many highly variable sources from the sample and would subsequently reduce the robustness of statistical tests on source properties.

2.2. Selection Method

We have identified a total of 133 AGNs that satisfy our selection criteria (see Table 1), 96 of which are also members of

TABLE 1
THE COMPLETE MOJAVE SAMPLE

Source (1)	Alias (2)	R.A. (J2000.0) (3)	Decl. (J2000.0) (4)	z (5)	Opt. Class. (6)	V Magnitude (7)	Radio Spectrum (8)	S_{VLBA} (Jy) (9)	γ-Ray ID (10)
0003−066	NRAO 005	00 06 13.8928	−06 23 35.3353	0.347	B	18.5	Flat	2.83	...
0007+106	III Zw 2	00 10 31.0058	+10 58 29.5041	0.0893	G	15.4	Flat	3.00*	...
0016+731	...	00 19 45.7864	+73 27 30.0174	1.781	Q	19.0	Flat	2.40*	...
0048−097	...	00 50 41.3173	−09 29 05.2102	...	B	17.4	Flat	2.70*	...
0059+581	...	01 02 45.7623	+58 24 11.1366	...	U	...	Flat	3.31	...
0106+013	...	01 08 38.7710	+01 35 00.3171	2.107	Q	18.4	Flat	2.97	...
0109+224	...	01 12 05.8247	+22 44 38.7861	...	B	15.7	Flat	1.65*	...
0119+115.............	...	01 21 41.5950	+11 49 50.4131	0.570	Q	19.7	Flat	2.00*	...
0133+476	DA 55	01 36 58.5948	+47 51 29.1000	0.859	Q	19.5	Flat	4.95	...
0202+149	4C +15.05	02 04 50.4139	+15 14 11.0434	0.405	Q^e	21.0	Flat	2.29	Y
0202+319	...	02 05 04.9253	+32 12 30.0956	1.466	Q	17.4	Flat	2.27	...
0212+735	...	02 17 30.8133	+73 49 32.6217	2.367	Q	20.0	Flat	2.69	...
0215+015	...	02 17 48.9547	+01 44 49.6990	1.715	B^a	16.1	Flat	3.40*	...
0224+671	4C +67.05	02 28 50.0514	+67 21 03.0292	...	U	...	Flat	2.60*	...
0234+285	CTD 20	02 37 52.4056	+28 48 08.9900	1.207	Q	19.3	Flat	4.04	P
0235+164	...	02 38 38.9301	+16 36 59.2747	0.940	B^a	15.5	Flat	1.62	Y
0238−084	NGC 1052	02 41 04.7985	−08 15 20.7518	0.0049	G	12.3	Flat	2.48	...
0300+470	4C +47.08	03 03 35.2422	+47 16 16.2754	...	B	17.0	Flat	1.70*	...
0316+413	3C 84	03 19 48.1601	+41 30 42.1030	0.0176	G	12.5	Flat	10.64	...
0333+321	NRAO 140	03 36 30.1075	+32 18 29.3423	1.263	Q	17.5	Flat	2.25	...
0336−019	CTA 26	03 39 30.9377	−01 46 35.8039	0.852	Q	18.4	Flat	3.44	Y
0403−132	...	04 05 34.0034	−13 08 13.6910	0.571	Q	17.1	Flat	2.30*	...
0415+379	3C 111	04 18 21.2770	+38 01 35.9000	0.0491	G	18.1	Steep	5.98	...
0420−014	...	04 23 15.8007	−01 20 33.0653	0.915	Q	17.0	Flat	10.60	Y
0422+004	...	04 24 46.8420	+00 36 06.3298	...	B	17.0	Flat	1.78	...
0430+052	3C 120	04 33 11.0955	+05 21 15.6194	0.0330	G	15.1	Flat	4.41	...
0446+112	...	04 49 07.6711	+11 21 28.5966	...	Q^b	20.0	Flat	2.25	P
0458−020	...	05 01 12.8098	−01 59 14.2562	2.291	Q	18.1	Flat	2.33	Y
0528+134	...	05 30 56.4167	+13 31 55.1495	2.070	Q	20.0	Flat	7.95	Y
0529+075	...	05 32 38.9985	+07 32 43.3458	...	U	...	Flat	1.63	...
0529+483	...	05 33 15.8657	+48 22 52.8078	1.162	Q	19.9	Flat	1.50*	P
0552+398	DA 193	05 55 30.8056	+39 48 49.1650	2.363	Q	18.3	Peaked	5.02	...
0605−085	...	06 07 59.6992	−08 34 49.9781	0.872	Q	17.6	Flat	2.80	...
0607−157	...	06 09 40.9495	−15 42 40.6726	0.324	Q	18.0	Flat	7.26	...
0642+449	OH 471	06 46 32.0259	+44 51 16.5901	3.408	Q	18.5	Peaked	4.31	...
0648−165	...	06 50 24.5818	−16 37 39.7250	...	U	...	Flat	2.68	...
0716+714	...	07 21 53.4484	+71 20 36.3633	...	B	15.5	Flat	2.58	Y
0727−115	...	07 30 19.1124	−11 41 12.6004	1.591	Q	20.3	Flat	5.31	...
0730+504	...	07 33 52.5205	+50 22 09.0620	0.720	Q	19.3	Flat	1.60*	...
0735+178	...	07 38 07.3937	+17 42 18.9982	...	B	16.2	Flat	1.64	Y
0736+017	...	07 39 18.0338	+01 37 04.6180	0.191	Q	16.5	Flat	2.58	...
0738+313	OI 363	07 41 10.7033	+31 12 00.2286	0.630	Q	16.1	Flat	2.87	...
0742+103	...	07 45 33.0595	+10 11 12.6924	2.624	Q	24.0	Peaked	1.50	...
0748+126	...	07 50 52.0457	+12 31 04.8281	0.889	Q	18.7	Flat	3.25	...
0754+100	...	07 57 06.6429	+09 56 34.8521	0.266	B	15.0	Flat	1.83	...
0804+499	...	08 08 39.6662	+49 50 36.5304	1.432	Q	18.3	Flat	3.60*	...
0805−077	...	08 08 15.5360	−07 51 09.8863	1.837	Q	19.8	Flat	2.00*	P
0808+019	...	08 11 26.7073	+01 46 52.2200	0.93	B	17.2	Flat	1.90*	...
0814+425	...	08 18 15.9996	+42 22 45.4149	...	B	18.2	Flat	2.60*	...
0823+033	...	08 25 50.3383	+03 09 24.5201	0.506	B	16.8	Flat	1.50*	...
0827+243	...	08 30 52.0861	+24 10 59.8204	0.941	Q	17.3	Flat	1.99	Y
0829+046	...	08 31 48.8769	+04 29 39.0853	0.180	B	16.4	Flat	4.20*	Y
0836+710	...	08 41 24.3652	+70 53 42.1730	2.218	Q	17.3	Flat	2.24	Y
0851+202	OJ 287	08 54 48.8749	+20 06 30.6408	0.306	B	15.4	Flat	4.12	Y
0906+015	4C +01.24	09 09 10.0915	+01 21 35.6176	1.018	Q	17.8	Flat	2.73	...
0917+624	...	09 21 36.2310	+62 15 52.1803	1.446	Q	19.5	Flat	2.00*	...
0923+392	4C +39.25	09 27 03.0139	+39 02 20.8519	0.698	Q	17.9	Flat	12.68	...
0945+408	...	09 48 55.3381	+40 39 44.5871	1.252	Q	18.4	Flat	1.59	...
0955+476	...	09 58 19.6716	+47 25 07.8425	1.873	Q	18.7	Flat	1.75	...
1036+054	...	10 38 46.7798	+05 12 29.0853	...	U	...	Flat	2.66	...
1038+064	...	10 41 17.1625	+06 10 16.9237	1.265	Q	16.7	Flat	1.85	...
1045−188	...	10 48 06.6206	−19 09 35.7269	0.595	Q	18.2	Flat	2.30*	...
1055+018	4C +01.28	10 58 29.6052	+01 33 58.8237	0.888	Q	18.3	Flat	5.30	...
1124−186.............	...	11 27 04.3924	−18 57 17.4416	1.048	Q	18.7	Flat	2.82	...

TABLE 1—*Continued*

Source (1)	Alias (2)	R.A. (J2000.0) (3)	Decl. (J2000.0) (4)	z (5)	Opt. Class. (6)	V Magnitude (7)	Radio Spectrum (8)	S_{VLBA} (Jy) (9)	γ-Ray ID (10)
1127−145............	. . .	11 30 07.0525	−14 49 27.3881	1.187	Q	16.9	Flat	3.39	P
1150+812	. . .	11 53 12.4991	+80 58 29.1545	1.250	Q	19.4	Flat	1.51	. . .
1156+295	4C +29.45	11 59 31.8339	+29 14 43.8269	0.729	Q	14.4	Flat	2.36	P
1213−172	. . .	12 15 46.7517	−17 31 45.4028	. . .	U	. . .	Flat	2.56	. . .
1219+044	. . .	12 22 22.5496	+04 13 15.7763	0.965	Q	18.0	Flat	1.50*	. . .
1222+216	. . .	12 24 54.4583	+21 22 46.3886	0.435	Q	17.5	Flat	1.76	Y
1226+023	3C 273	12 29 06.6997	+02 03 08.5981	0.158	Q	12.9	Flat	41.40	Y
1228+126	M87	12 30 49.4233	+12 23 28.0439	0.0044	G	12.9	Steep	2.97	. . .
1253−055	3C 279	12 56 11.1665	−05 47 21.5245	0.538	Q	17.8	Flat	24.89	Y
1308+326	. . .	13 10 28.6638	+32 20 43.7829	0.997	Q	15.2	Flat	3.98	. . .
1324+224	. . .	13 27 00.8613	+22 10 50.1630	1.400	Q	18.9	Flat	1.50*	P
1334−127	. . .	13 37 39.7827	−12 57 24.6932	0.539	Q	19.0	Flat	8.87	Y
1413+135	. . .	14 15 58.8174	+13 20 23.7126	0.247	B	20.5	Flat	1.72	. . .
1417+385	. . .	14 19 46.6137	+38 21 48.4752	1.832	Q	19.3	Flat	1.70*	P
1458+718	3C 309.1	14 59 07.5838	+71 40 19.8677	0.904	Q	16.8	Steep	1.50	. . .
1502+106	4C +10.39	15 04 24.9797	+10 29 39.1986	1.833	Q	18.6	Flat	1.95	. . .
1504−166	. . .	15 07 04.7869	−16 52 30.2673	0.876	Q	18.5	Flat	2.03	P
1510−089	. . .	15 12 50.5329	−09 05 59.8295	0.360	Q	16.5	Flat	2.93	Y
1538+149	4C +14.60	15 40 49.4915	+14 47 45.8848	0.605	B[a]	17.3	Flat	2.20*	. . .
1546+027	. . .	15 49 29.4368	+02 37 01.1634	0.412	Q	17.8	Flat	2.83	. . .
1548+056	4C +05.64	15 50 35.2692	+05 27 10.4482	1.422	Q	19.5	Flat	2.93	. . .
1606+106	4C +10.45	16 08 46.2031	+10 29 07.7758	1.226	Q	18.7	Flat	1.93	Y
1611+343	DA 406	16 13 41.0642	+34 12 47.9090	1.401	Q	18.1	Flat	4.52	Y
1633+382	4C +38.41	16 35 15.4929	+38 08 04.5006	1.807	Q	17.7	Flat	4.29	Y
1637+574	. . .	16 38 13.4562	+57 20 23.9791	0.751	Q	16.9	Flat	1.88	. . .
1638+398	NRAO 512	16 40 29.6327	+39 46 46.0285	1.666	Q	19.4	Flat	1.61	. . .
1641+399	3C 345	16 42 58.8099	+39 48 36.9939	0.594	Q	16.0	Flat	8.73	. . .
1655+077	. . .	16 58 09.0114	+07 41 27.5407	0.621	Q	20.0	Flat	2.09	. . .
1726+455	. . .	17 27 27.6508	+45 30 39.7313	0.714	Q	18.1	Flat	2.18	. . .
1730−130	NRAO 530	17 33 02.7057	−13 04 49.5482	0.902	Q	19.5	Flat	10.97	Y
1739+522	4C +51.37	17 40 36.9778	+52 11 43.4075	1.379	Q	18.7	Flat	1.77	Y
1741−038	. . .	17 43 58.8561	−03 50 04.6166	1.057	Q	20.4	Flat	7.01	Y
1749+096	4C +09.57	17 51 32.8185	+09 39 00.7285	0.320	B[a]	16.8	Flat	5.58	. . .
1751+288	. . .	17 53 42.4736	+28 48 04.9390	. . .	U	. . .	Flat	2.02	. . .
1758+388	. . .	18 00 24.7653	+38 48 30.6975	2.092	Q	18.0	Peaked	1.75	. . .
1800+440	. . .	18 01 32.3148	+44 04 21.9003	0.663	Q	17.9	Flat	1.50	. . .
1803+784	. . .	18 00 45.6839	+78 28 04.0185	0.680	B[a]	15.9	Flat	2.54	. . .
1823+568	4C +56.27	18 24 07.0683	+56 51 01.4908	0.663	B[a]	19.3	Flat	2.31	. . .
1828+487	3C 380	18 29 31.7388	+48 44 46.9710	0.692	Q	16.8	Steep	2.01	. . .
1849+670	. . .	18 49 16.0723	+67 05 41.6799	0.657	Q	16.9	Flat	1.74	. . .
1928+738	4C +73.18	19 27 48.4951	+73 58 01.5699	0.303	Q	16.1	Flat	3.93	. . .
1936−155	. . .	19 39 26.6577	−15 25 43.0583	1.657	Q	20.3	Flat	2.00*	P
1957+405	Cygnus A	19 59 28.3566	+40 44 02.0965	0.0561	G	15.1	Steep	1.68	. . .
1958−179	. . .	20 00 57.0904	−17 48 57.6725	0.652	Q	18.6	Flat	2.67	. . .
2005+403	. . .	20 07 44.9448	+40 29 48.6041	1.736	Q	19.0	Flat	2.82	. . .
2008−159	. . .	20 11 15.7109	−15 46 40.2538	1.180	Q	18.3	Peaked	2.14	. . .
2021+317	4C +31.56	20 23 19.0127	+31 53 02.3059	. . .	U	. . .	Flat	2.16	. . .
2021+614	. . .	20 22 06.6816	+61 36 58.8047	0.227	G	19.0	Flat	2.73	. . .
2037+511	3C 418	20 38 37.0347	+51 19 12.6626	1.687	Q	21.0	Flat	2.33	. . .
2121+053	. . .	21 23 44.5173	+05 35 22.0932	1.941	Q	20.4	Flat	2.57	. . .
2128−123	. . .	21 31 35.2617	−12 07 04.7958	0.501	Q	16.1	Flat	3.17	. . .
2131−021	4C −02.81	21 34 10.3096	−01 53 17.2389	1.285	B[a]	19.0	Flat	2.21	. . .
2134+004	. . .	21 36 38.5863	+00 41 54.2133	1.932	Q	16.8	Peaked	6.34	. . .
2136+141	OX 161	21 39 01.3092	+14 23 35.9919	2.427	Q	18.9	Flat	2.75	. . .
2145+067	4C +06.69	21 48 05.4586	+06 57 38.6042	0.999	Q	16.5	Flat	10.37	. . .
2155−152	. . .	21 58 06.2819	−15 01 09.3280	0.672	Q	18.3	Flat	2.11	. . .
2200+420	BL Lac	22 02 43.2913	+42 16 39.9799	0.0686	B	14.7	Flat	5.67	Y
2201+171	. . .	22 03 26.8936	+17 25 48.2478	1.076	Q	19.5	Flat	2.01	. . .
2201+315	4C +31.63	22 03 14.9757	+31 45 38.2699	0.298	Q	15.6	Flat	3.28	. . .
2209+236	. . .	22 12 05.9663	+23 55 40.5438	1.125	Q	20.7	Flat	1.62	Y
2216−038	. . .	22 18 52.0377	−03 35 36.8794	0.901	Q	16.4	Flat	2.54	. . .
2223−052	3C 446	22 25 47.2592	−04 57 01.3907	1.404	Q	18.4	Flat	6.57	. . .
2227−088	PHL 5225	22 29 40.0843	−08 32 54.4354	1.562	Q	18.1	Flat	2.00	. . .
2230+114	CTA 102	22 32 36.4089	+11 43 50.9041	1.037	Q	17.3	Flat	4.86	P

TABLE 1—*Continued*

Source (1)	Alias (2)	R.A. (J2000.0) (3)	Decl. (J2000.0) (4)	z (5)	Opt. Class. (6)	V Magnitude (7)	Radio Spectrum (8)	S_{VLBA} (Jy) (9)	γ-Ray ID (10)
2243−123	...	22 46 18.2319	−12 06 51.2773	0.630	Q	16.5	Flat	2.56	...
2251+158	3C 454.3	22 53 57.7479	+16 08 53.5608	0.859	Q	16.1	Flat	12.08	Y
2331+073	...	23 34 12.8281	+07 36 27.5520	...	U	...	Flat	1.50*	...
2345−167	...	23 48 02.6085	−16 31 12.0220	0.576	Q	18.4	Flat	2.54	...
2351+456	4C +45.51	23 54 21.6802	+45 53 04.2365	1.986	Q	20.6	Flat	1.80	P

Notes.—Columns are as follows: (1) IAU name (B1950.0); (2) other name; (3) right ascension (J2000.0); (4) declination (J2000.0); (5) redshift from Véron-Cetty & Véron (2003) (the redshift of 0742+103 is from Best et al. [2003], and that of 0808+019 is from Jackson et al. [2002]); (6) optical classification according to the Véron-Cetty & Véron (2003) catalog, where Q is quasar, B is BL Lac object, G is active galaxy, and U is unidentified; (7) optical V magnitude from Véron-Cetty & Véron (2003) catalog; (8) description of radio spectrum from Kellermann et al. (2004); (9) maximum 2 cm total cleaned VLBA flux density at any epoch during 1994–2003 (values with asterisks are inferred from single-dish observations; see § 2.1); (10) EGRET gamma-ray source identification according to Mattox et al. (2001) and Sowards-Emmerd et al. (2003, 2004), where Y is highly probable identification and P is probable identification. Units of right ascension are hours, minutes, and seconds, and units of declination are degrees, arcminutes, and arcseconds. Table 1 is also available in machine-readable form in the electronic edition of the *Astronomical Journal*.

[a] Source classified as a quasar in the Véron-Cetty & Véron (2003) catalog.
[b] Source classified as a possible BL Lac object in the Véron-Cetty & Véron (2003) catalog.
[c] Source classified as a galaxy in the Véron-Cetty & Véron (2003) catalog.

the VLBA 2 cm Survey. The procedure used in arriving at this list was somewhat complex because of the limited VLBA monitoring data that were available. Our first step was to compile a candidate list of all known AGNs with an observed or extrapolated 15 GHz *single-dish* flux density greater than 1.5 (or 2) Jy. We consulted the Kühr 1 Jy catalog (Kühr et al. 1981; Stickel et al. 1994), the VLA calibrator database,[3] the Parkes Half-Jansky flat-spectrum sample (Drinkwater et al. 1997), and the Jodrell Bank–VLA Astrometric Survey (Browne et al. 2003) for this purpose. The latter is complete to within 2°.5 of the Galactic plane for northern declinations. Since these combined catalogs are complete over our defined sky region at 5 GHz, the only potentially missing sources at this stage were those AGNs with spectra peaked at frequencies higher than 5 GHz and variable sources that happened to be weak at the time of the catalog selection. To alleviate the former bias, we checked the *Wilkinson Microwave Anisotropy Probe* (*WMAP*) catalog (Bennett et al. 2003), the 22 GHz VLBI survey of Moellenbrock et al. (1996), and the high-frequency peaked samples of Teräsranta et al. (2001) and Dallacasa et al. (2000) for sources that met the single-dish flux density criteria. We also added any variable sources from the University of Michigan Radio Astronomy Observatory (UMRAO) and RATAN AGN monitoring programs (Aller et al. 2003; Kovalev et al. 2002) that had sufficient 15 GHz flux density at any epoch during the 10 yr window. The latter program has observed approximately 3000 radio sources with flux densities exceeding 100 mJy since 1995.

The second stage of source selection was to eliminate from the candidate list all extended sources whose correlated VLBA flux densities were weaker than our cutoff. Past surveys (e.g., the Caltech–Jodrell Bank Flat-Spectrum [CJF] survey, Taylor et al. 1996) have accomplished this by using a spectral flatness criterion, which assumes that the weak-core sources will have steep radio spectra because of their extended structure. We did not adopt this method for our survey, since we found that some nearby AGNs with steep spectra but sufficiently bright cores (e.g., M87 and 3C 380) were incorrectly rejected. We instead used the measured VLBA flux densities from the VLBA 2 cm Survey as the main criterion for MOJAVE survey membership. If a candidate source still did not meet the VLBA flux density criterion at four different epochs within the time window (or had

fewer than four VLBA epochs), we determined the VLBA–to–single-dish flux density ratio using near-simultaneous UMRAO and VLBA observations (tabulated in Kovalev et al. 2005). We thus used this to estimate the VLBA 15 GHz flux density based on RATAN or UMRAO observations taken during the 10 yr window.

2.3. General Properties

In Table 1 we summarize the general properties of the MOJAVE sample. The coordinate positions in columns (3) and (4) were obtained from the NASA/IPAC Extragalactic Database (NED) and represent the phase center of the VLBA observations. The map centers in Figure 1 are slightly offset from these coordinates in most cases because of the self-calibration technique. The optical identifications in column (6) are from Véron-Cetty & Véron (2003), with exceptions as noted. The BL Lac objects that Véron-Cetty & Véron (2003) have reclassified as quasars have, on occasion, displayed emission lines slightly wider than the nominal 5 Å limit. Since these are still much narrower than those typically found in quasars, we retain the BL Lac classifications for these objects. We list the optical V magnitude from Véron-Cetty & Véron (2003) in column (7) and point out that these are highly variable with time. The general descriptions of the radio spectral shape in column (8) are from Kellermann et al. (2004). All but 11 sources have flat overall radio spectra, which we define as a spectral index flatter than −0.5 at any frequency between 0.6 and 22 GHz. The five steep-spectrum sources in the sample have strong extended emission on arcsecond scales that dominates the integrated spectrum, but their parsec-scale emission still meets our selection criteria. The six peaked-spectrum sources have no known radio emission on arcsecond scales (with the exception of 2134+004; Stanghellini et al. 1998). We do not include 0738+313 and 1127−145 in the peaked-spectrum category, as they have variable radio spectra that are occasionally flat (Kovalev et al. 2002).

In column (9) of Table 1 we list the strongest measured 15 GHz VLBA flux density during the period 1994–2003. Those values with asterisks are estimated from single-dish measurements as described in § 2.2. Column (10) indicates whether the AGN has been identified as a likely counterpart to a $\gtrsim$30 MeV gamma-ray source detected by the EGRET instrument on board the *Compton Gamma-Ray Observatory*. A "Y" indicates a highly probable EGRET identification according to Mattox et al. (2001) and

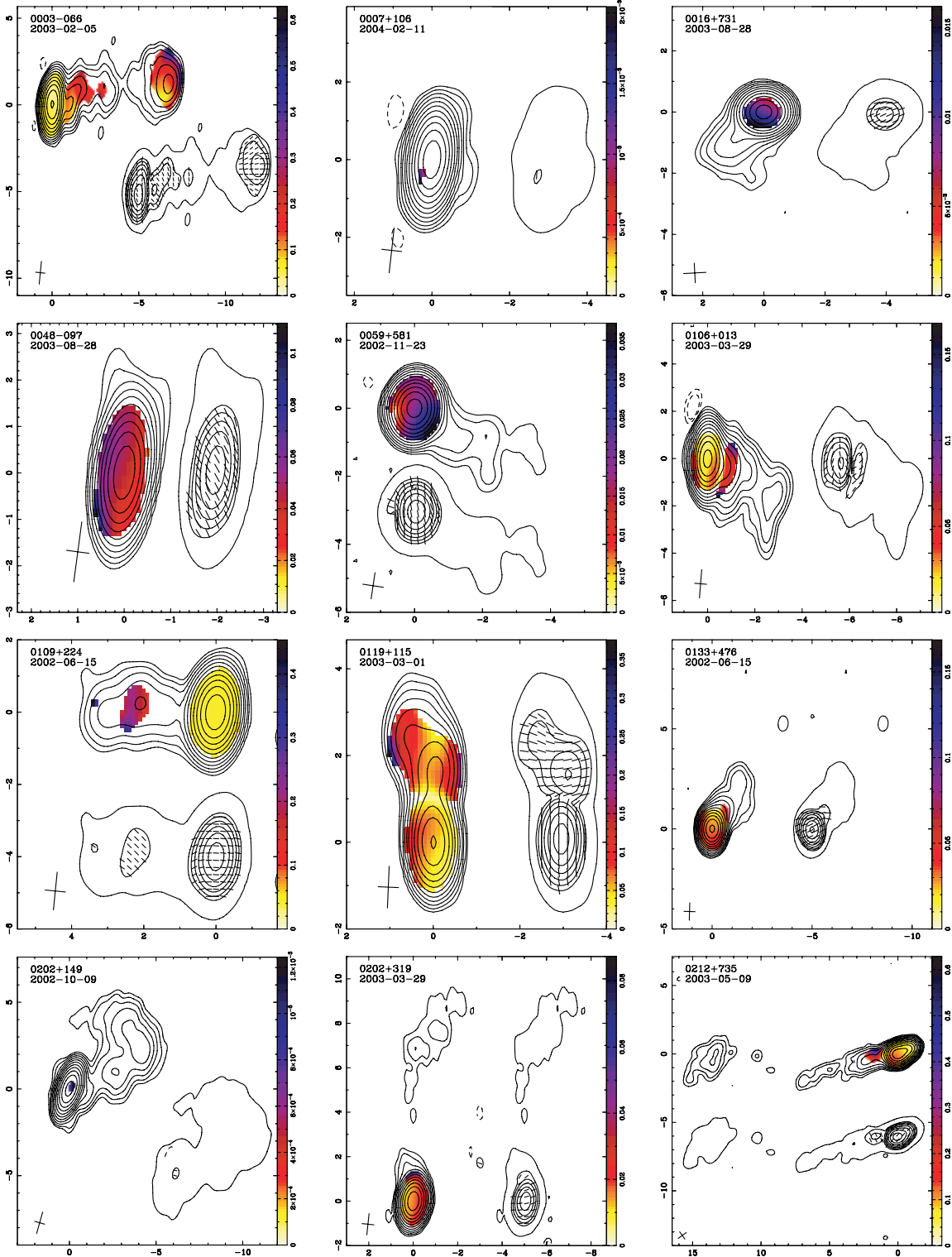[3] The VLA calibrator database can be found at http://www.vla.nrao.edu/astro/.

FIG. 1.—First-epoch 15 GHz VLBA images of the MOJAVE AGN sample. Each panel contains two images of the same source (arbitrarily offset), the first consisting of total intensity (Stokes *I*) contours in successive integer powers of 2 times the lowest contour (see Table 3), with linear fractional polarization overlaid according to the color wedge. A single negative *I* contour equal to the base contour is also plotted. The second image includes the lowest positive *I* contour from the first image, and linearly polarized intensity contours, also in increasing powers of 2. The cross indicates the FWHM dimensions and orientation of the restoring beam, and the short bars indicate the electric polarization vector directions. The coordinate origin generally lies at the position of the brightest feature in the *I* image because of the self-calibration technique.
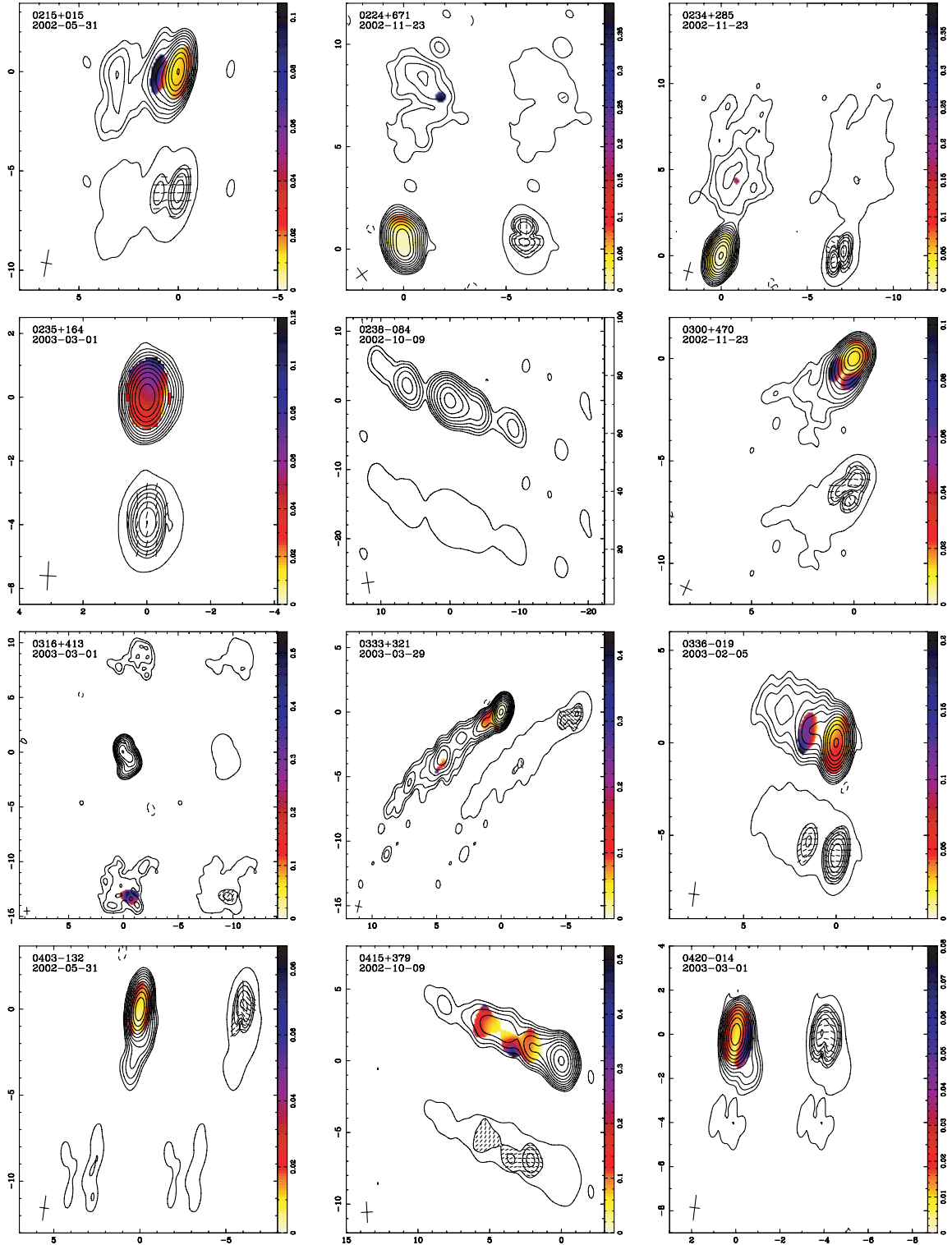
FIG. 1.—Continued
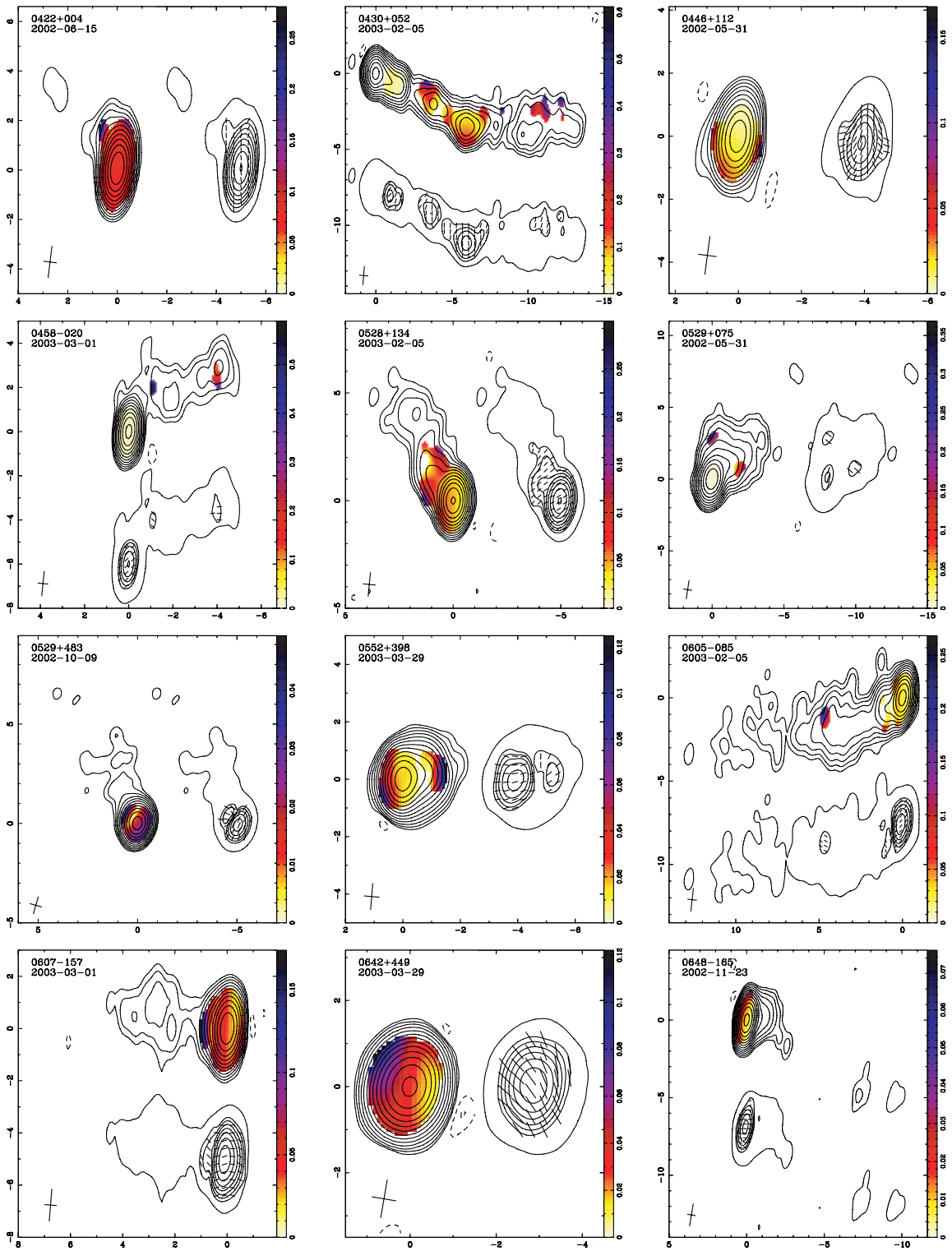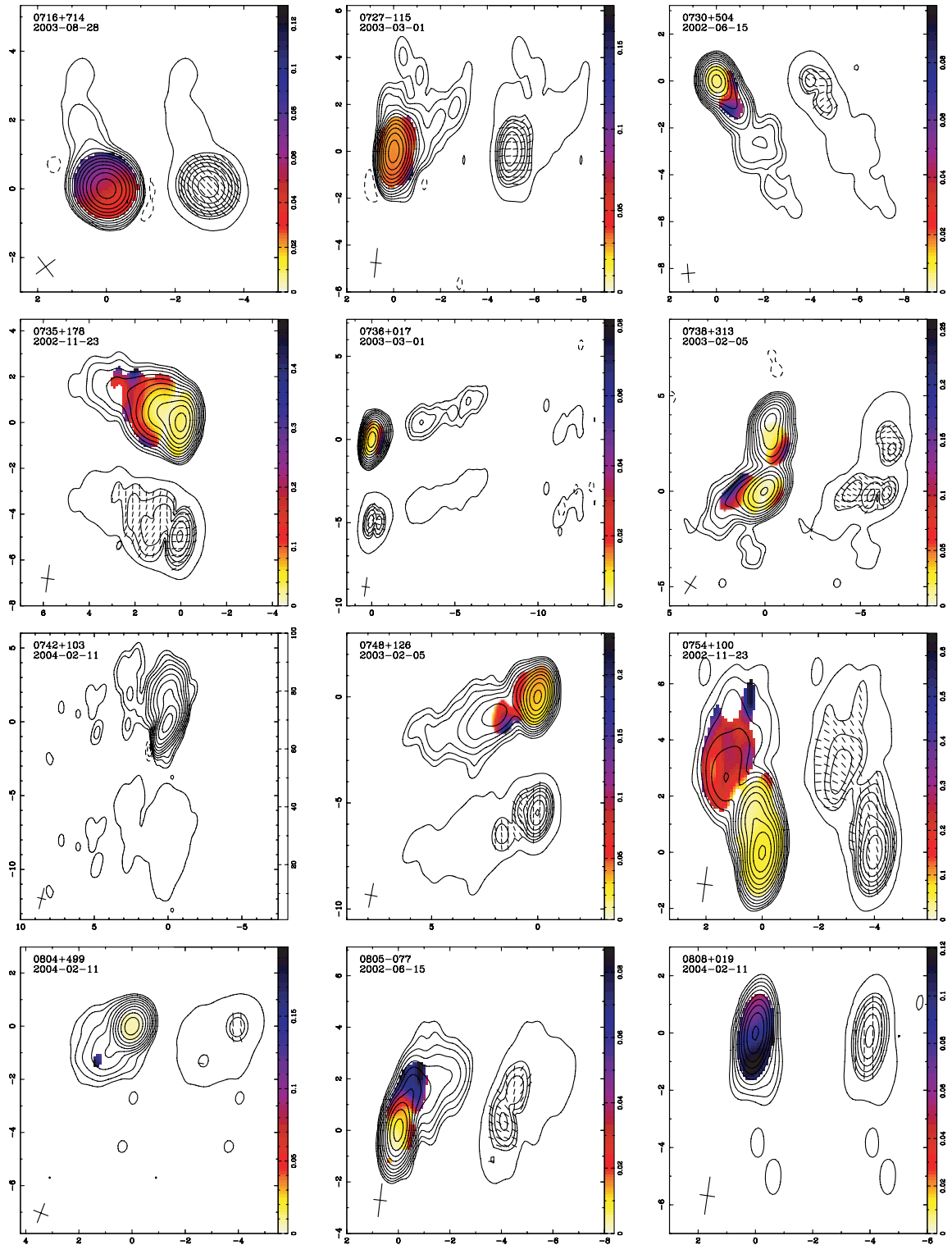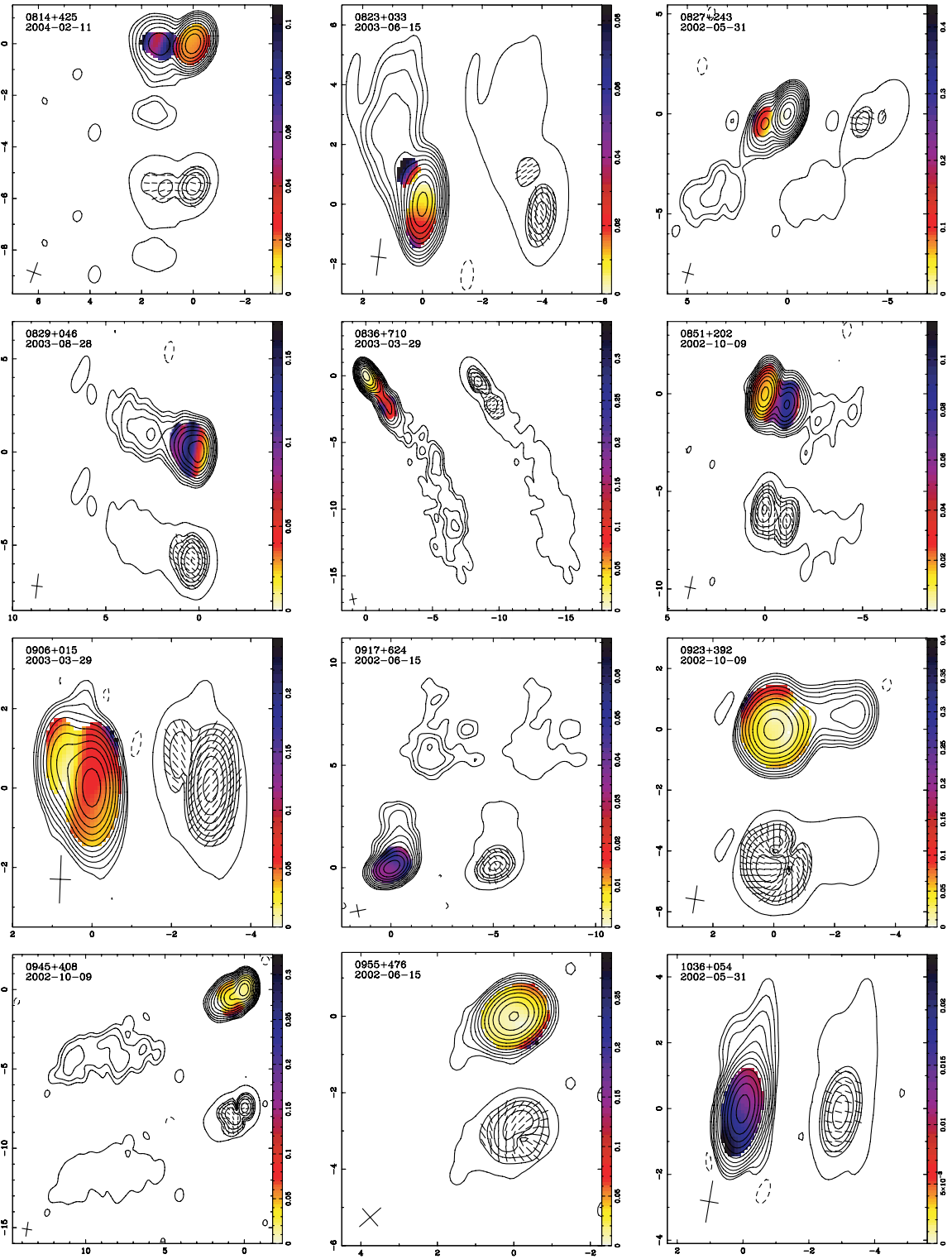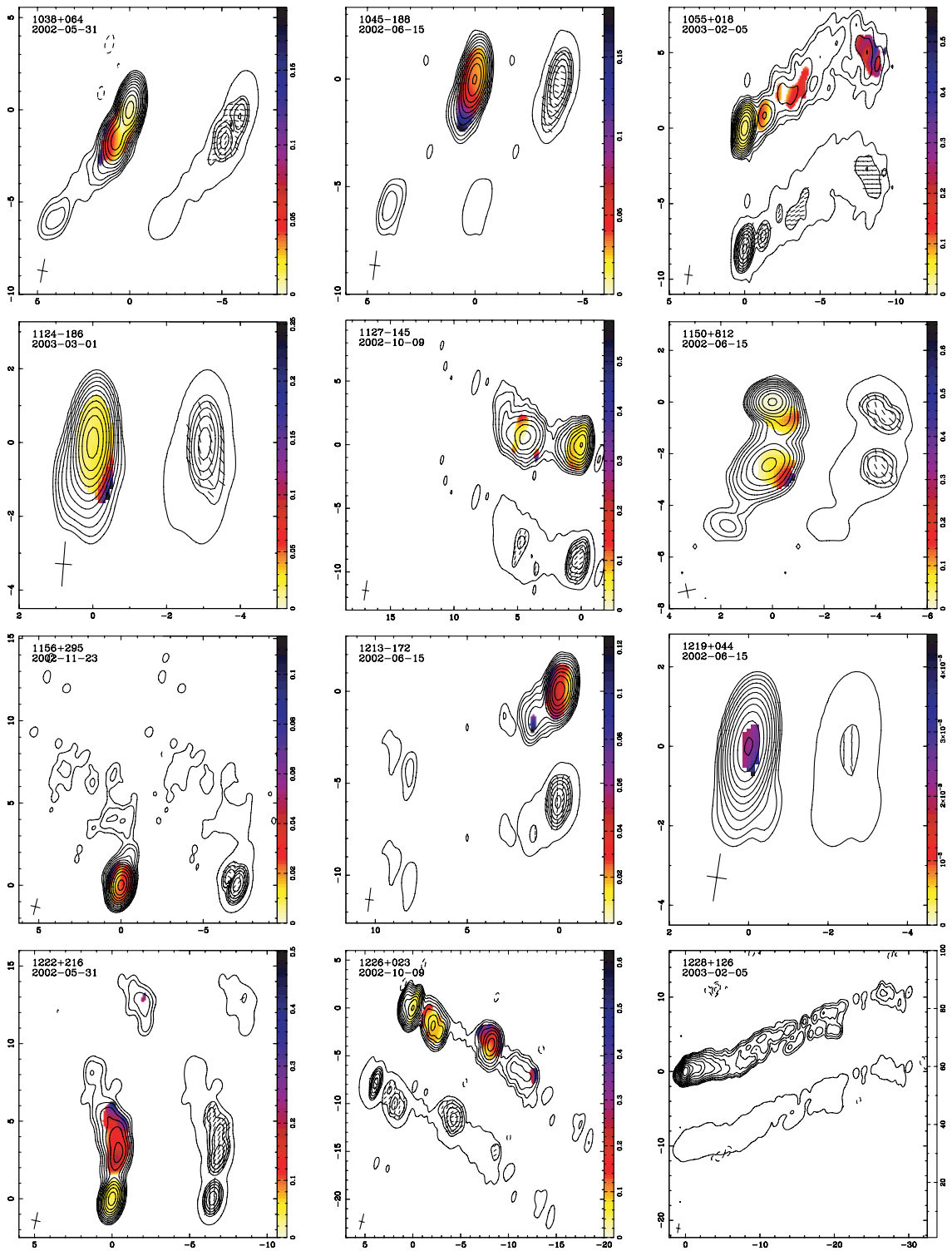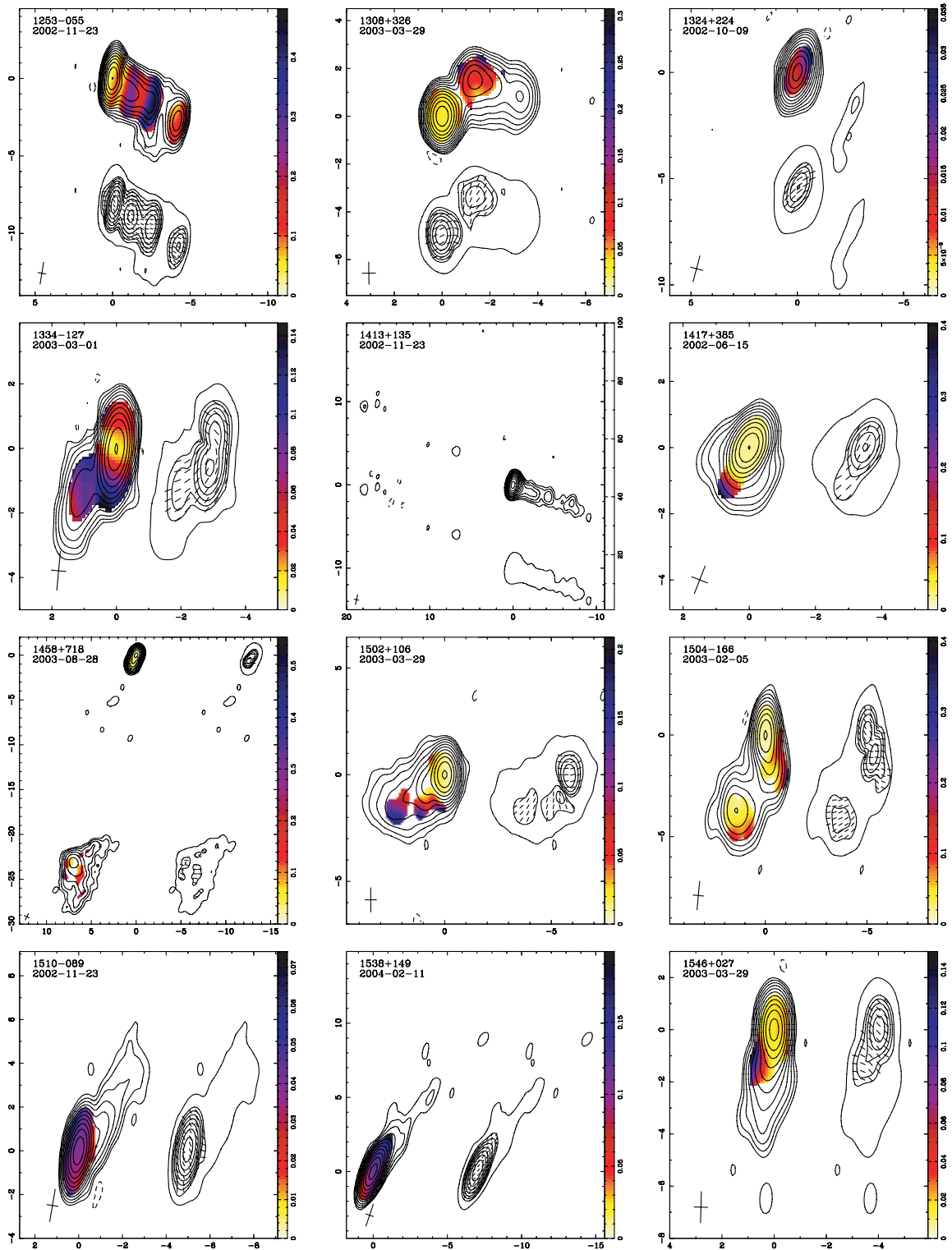
1395

FIG. 1.—*Continued*

FIG. 1.—*Continued*

0814+425
2004-02-11

0823+033
2003-06-15

0827+243
2002-05-31

0829+046
2003-08-28

0836+710
2003-03-29

0851+202
2002-10-09

0906+015
2003-03-29

0917+624
2002-06-15

0923+392
2002-10-09

0945+408
2002-10-09

0955+476
2002-06-15

1036+054
2002-05-31

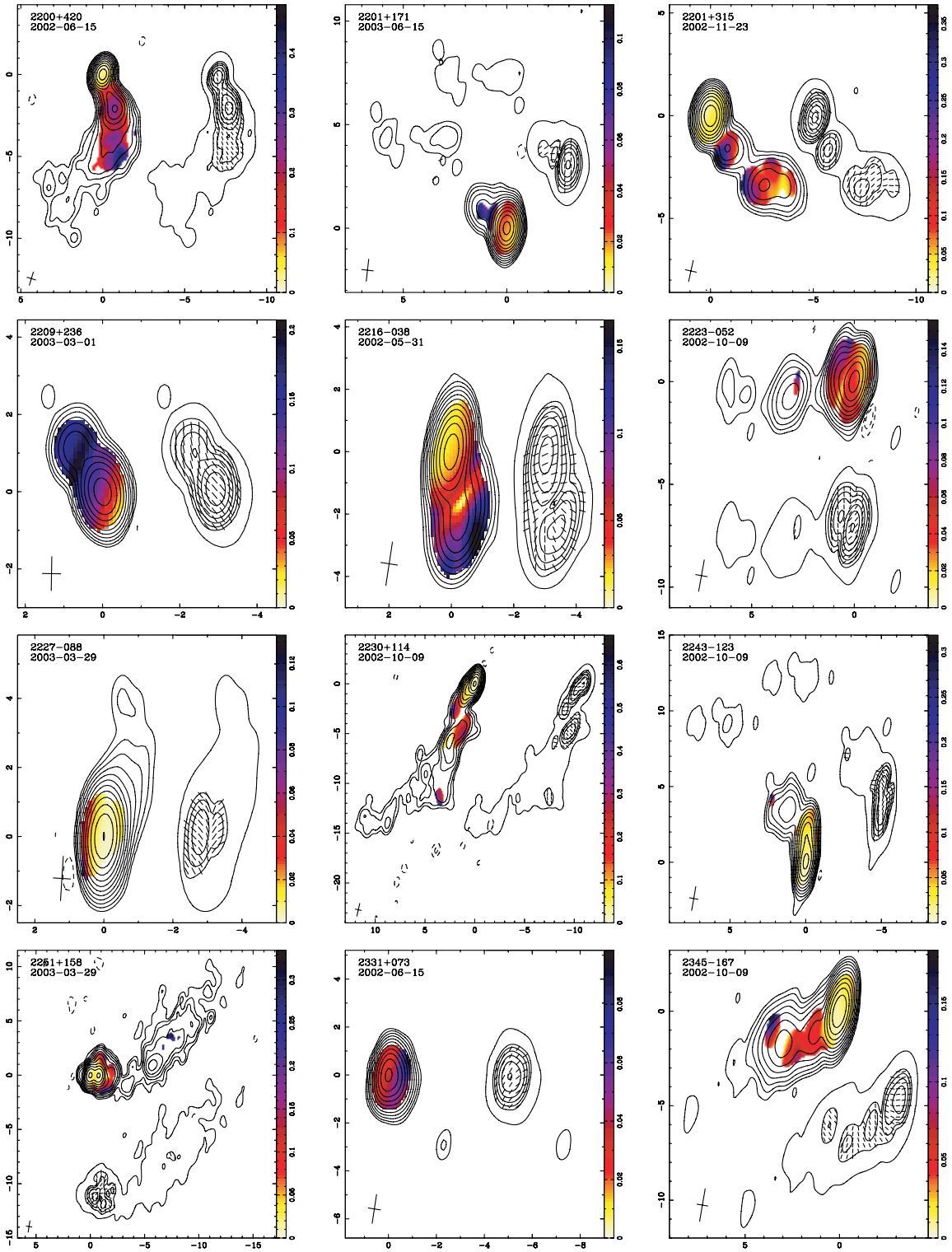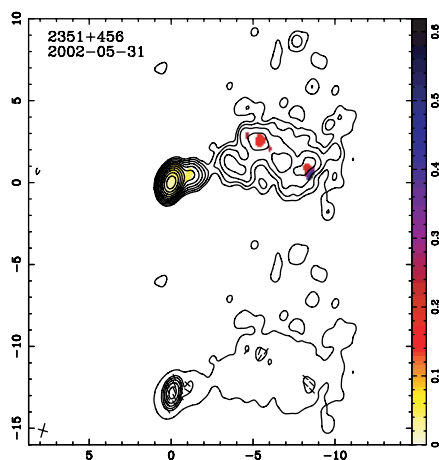Fig. 1.—*Continued*

FIG. 1.—*Continued*

FIG. 1.—*Continued*

FIG. 1.—*Continued*

1401
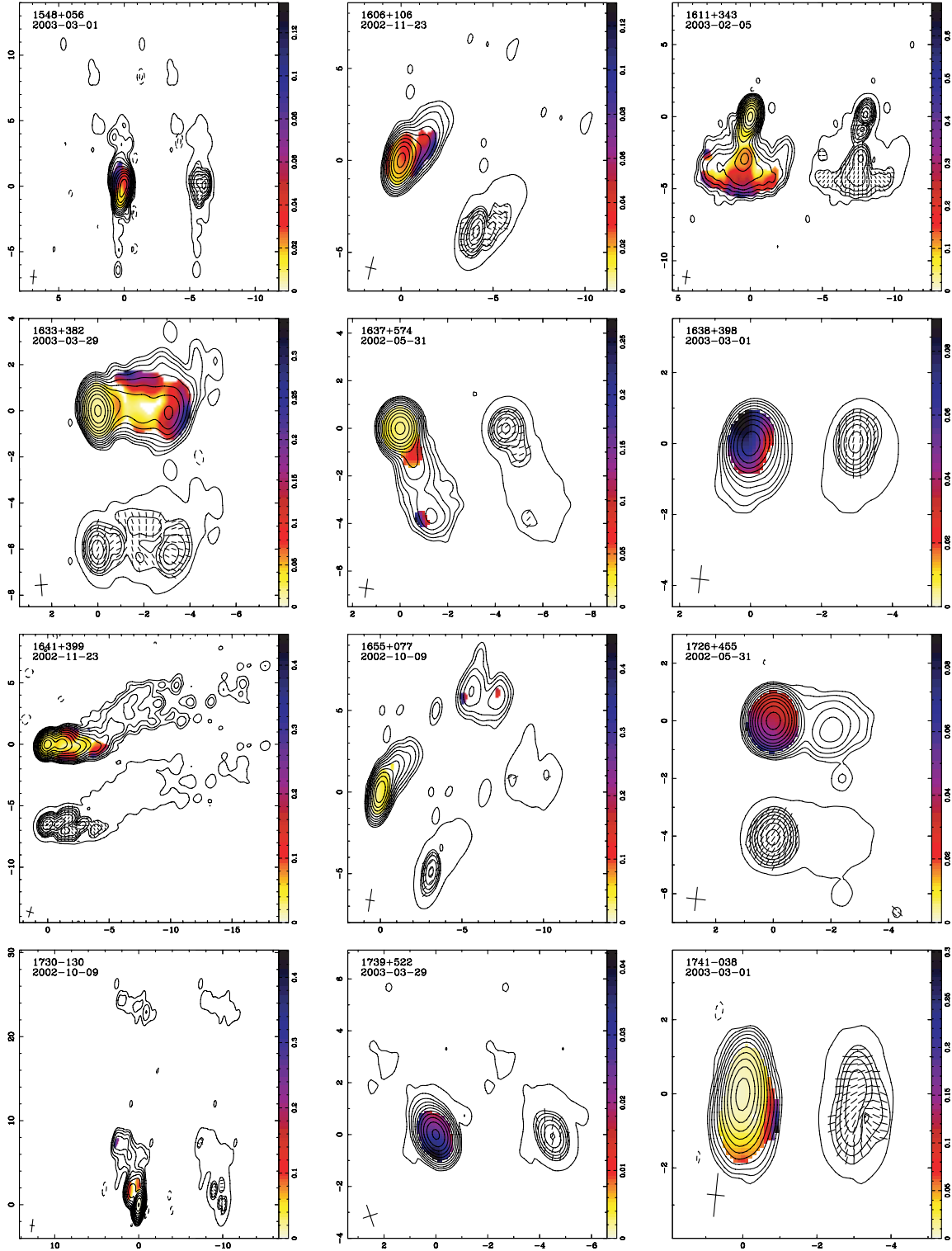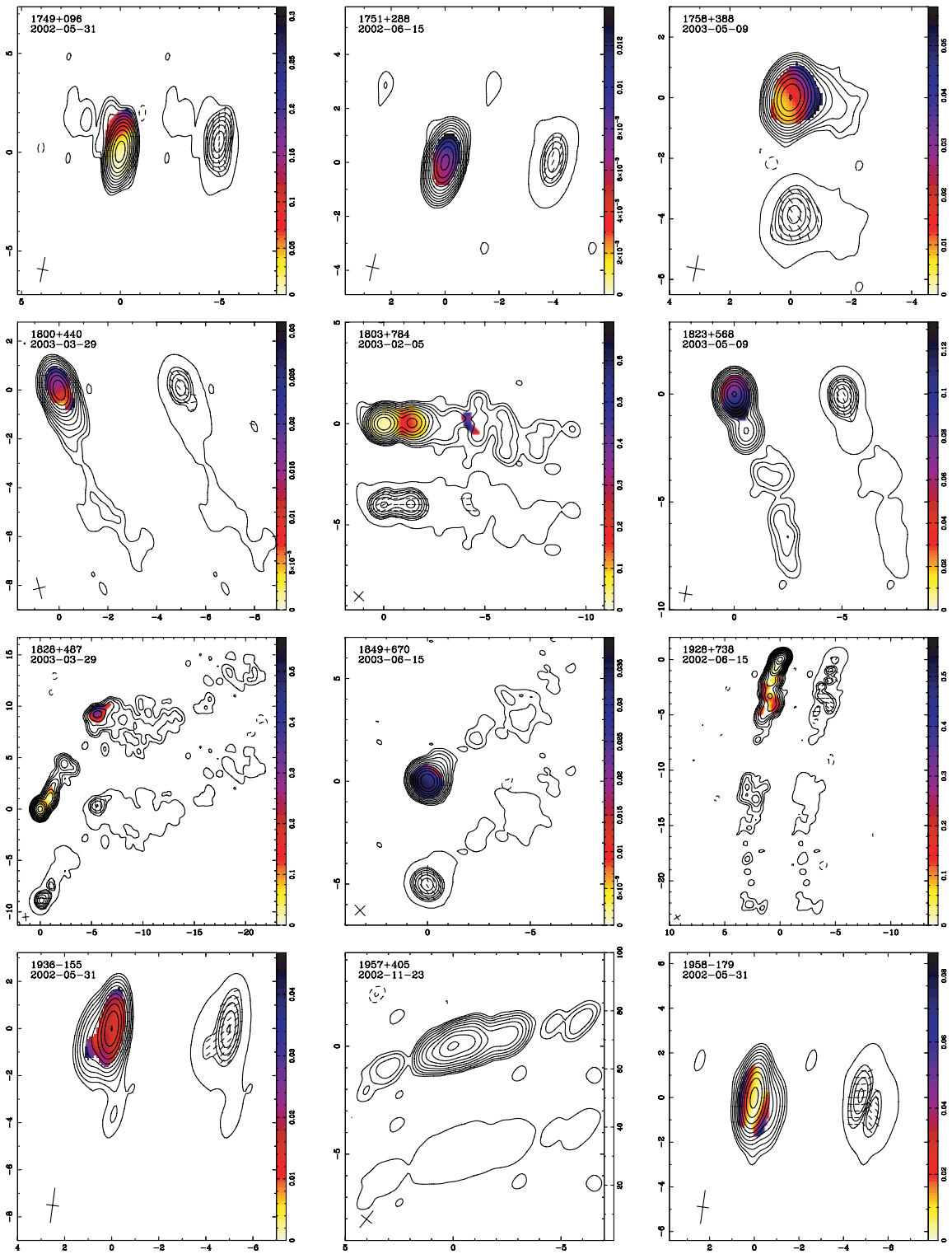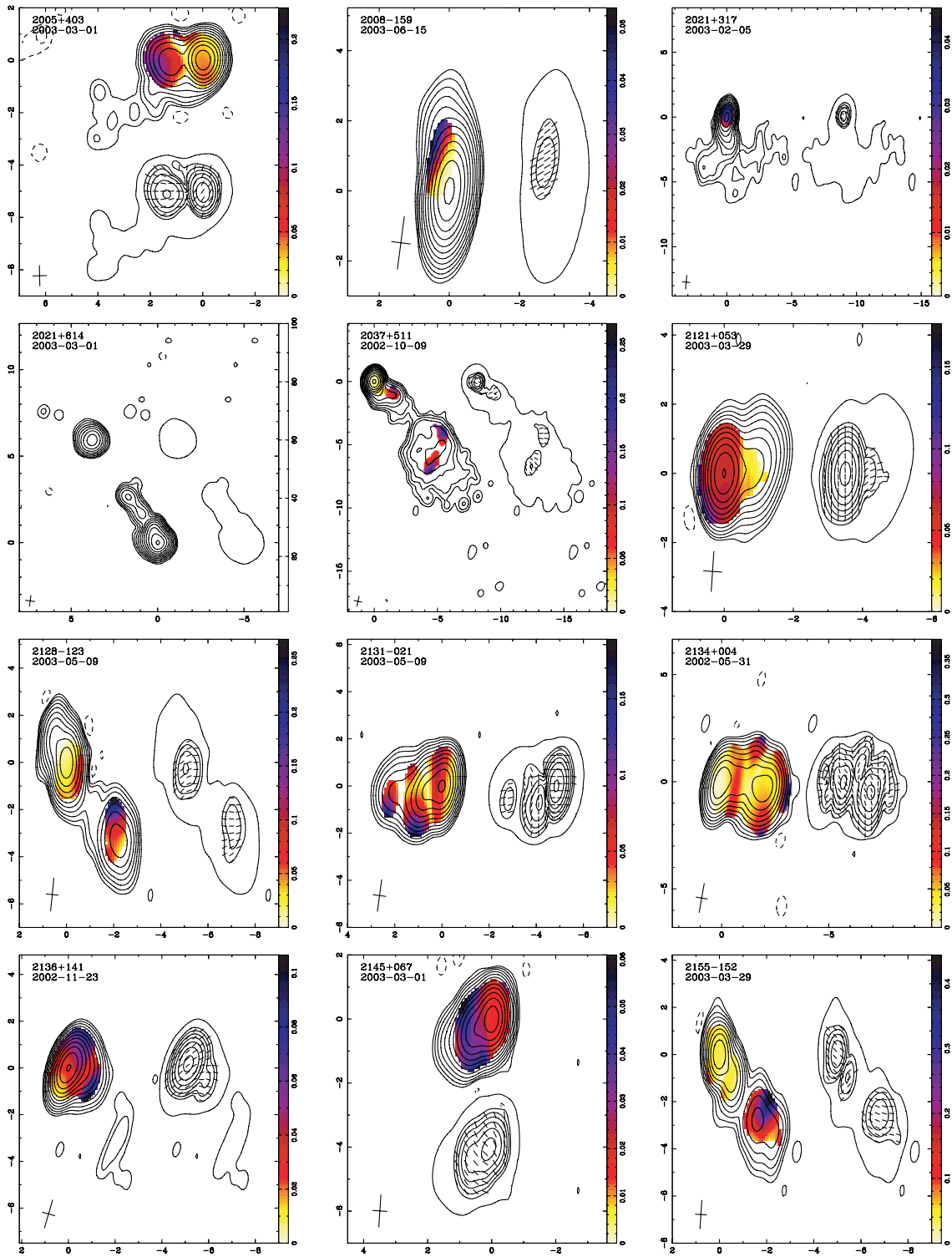
FIG. 1.—*Continued*

FIG. 1.—*Continued*

FIG. 1.—*Continued*

Fig. 1.—*Continued*

Sowards-Emmerd et al. (2003, 2004). Hereafter we refer to these as EGRET sources. A "P" indicates a less probable identification according to these authors and Thompson et al. (1993), and we will refer to these as probable EGRET sources. There are some disagreements in the literature regarding these probable EGRET sources, with 0234+285, 1156+295, and 2230+114 being considered as EGRET sources by Mattox et al. (2001), while 0446+112, 0529+483, and 1936−155 are considered as EGRET sources by Sowards-Emmerd et al. (2003, 2004). Mattox et al. (2001) do not consider 0805−077, 1127−145, 1324+224, 1417+385, and 1504−166 to be probable EGRET sources.

An overall summary of the optical and EGRET identifications for the MOJAVE sample is given in Table 2. Optical counterparts have been identified for 93% of the sample, and the redshift data are currently 86% complete. The sample is dominated by quasars, with the weak-lined BL Lac objects and radio galaxies making up 17% and 6% of the sample, respectively.

3. VLBA OBSERVATIONS AND DATA REDUCTION

3.1. *Data Calibration*

The first epoch of MOJAVE observations took place on 2002 May 31 using the VLBA. In this paper we present data obtained from this and 10 subsequent 24 hr MOJAVE sessions, up to and including 2004 February 11. All 10 VLBA antennas were used at a central observing frequency of 15.366 GHz. The data were recorded in eight baseband channels (intermediate frequencies [IFs]), each of 8 MHz bandwidth using 1 bit sampling. Both right- and left-hand polarizations were recorded simultaneously in IF pairs, giving a total observing bandwidth of 32 MHz in each polarization. During each observing session, short-duration (roughly 7 minute) scans of 18 MOJAVE sources were interleaved in order to span the widest possible range of hour angle and to obtain maximum parallactic angle and (u, v)-plane coverage. The total

integration time on each source was approximately 65 minutes. There was no need to observe any additional calibrators, since all the target sources were strong and compact.

The data were edited and calibrated at NRAO and Purdue University following the standard methods described in the AIPS Cookbook. The individual IFs were kept separate throughout the processing and were only averaged together when making the final Stokes images. This was necessary, since the polarization leakage terms at each antenna usually differ slightly among the IFs. A total of 80 leakage terms (four IFs times two circular polarization hands at 10 antennas) were determined at each epoch by running the task LPCAL on all sources and by taking the median solution values after removing obvious outliers. We determined the relative instrumental electric vector position angle (EVPA) rotation between epochs by comparing the individual leakage term solutions over time (Gomez et al. 2002). With very few exceptions, these remained very stable over periods of up to 1 yr, and based on the scatter we consider our relative EVPA error between epochs to be less than 2°. The leakage term method only gives relative EVPA corrections between epochs and still requires an absolute correction to establish the EVPA directions on the sky. This was obtained by comparing the VLBA EVPAs of the most compact MOJAVE sources with single-dish values obtained at the UMRAO. The latter observations were carried out typically within a week of the VLBA sessions. The systematic error in the absolute EVPAs is dominated by the nonsimultaneity of the observations and possible polarized structure not sampled by the VLBA. Based on the single-dish comparisons, we estimate that our absolute EVPA values are accurate to within 5°.

3.2. *Imaging*

We used the Caltech DIFMAP package (Pearson et al. 1994) to produce Stokes I, Q, and U images of each source from the

TABLE 2
Optical and EGRET Gamma-Ray Classifications of the MOJAVE Sample

Gamma-Ray Classification	Quasars	BL Lac Objects	Radio Galaxies	Unidentified	Total
EGRET..	20	6	0	0	26
Probable EGRET	12	0	0	0	12
Non-EGRET.................................	62	16	8	9	95
Total	94	22	8	9	133

TABLE 3
SUMMARY OF 15 GHz IMAGE PARAMETERS

Source (1)	Epoch (2)	B_{maj} (mas) (3)	B_{min} (mas) (4)	B_{PA} (deg) (5)	I_{tot} (Jy) (6)	I_{peak} (Jy beam^{-1}) (7)	P_{tot} (mJy) (8)	EVPA$_{tot}$ (deg) (9)	I_{base} (mJy beam^{-1}) (10)	P_{base} (mJy beam^{-1}) (11)	Scale (pc mas^{-1}) (12)
0003−066	2003 Feb 5	1.32	0.54	−5	2.83	1.83	101	17	1.7	1.7	4.9
0007+106	2004 Feb 11	1.16	0.51	−6	1.38	1.35	2	10	0.8	0.7	1.7
0016+731	2003 Aug 28	0.74	0.64	−87	1.07	1.01	9	108	0.7	1.7	8.4
0048−097	2003 Aug 28	1.30	0.49	−8	0.74	0.70	30	28	0.8	1.2	...
0059+581	2002 Nov 23	0.78	0.62	−9	3.30	3.16	63	11	1.1	1.2	...
0106+013	2003 Mar 29	1.20	0.51	−5	2.86	2.13	35	178	0.8	2.3	8.3
0109+224	2002 Jun 15	1.05	0.56	−6	1.01	0.93	43	86	0.5	0.9	...
0119+115.......	2003 Mar 1	0.96	0.47	−2	1.25	0.87	38	179	0.8	1.1	6.5
0133+476	2002 Jun 15	0.87	0.56	−2	4.48	4.20	140	115	1.8	1.9	7.7
0202+149	2002 Oct 9	1.28	0.60	−16	1.60	1.23	1	84	0.9	0.9	5.4
0202+319	2003 Mar 29	0.96	0.54	−6	2.27	2.10	36	103	1.2	1.3	8.5
0212+735	2003 May 9	0.74	0.66	−54	2.43	1.25	192	139	0.7	1.5	8.2
0215+015	2002 May 31	1.36	0.54	−10	0.90	0.75	14	93	0.7	0.8	8.5
0224+671	2002 Nov 23	0.77	0.65	36	1.30	0.68	6	126	0.7	0.8	...
0234+285	2002 Nov 23	1.08	0.55	−15	4.04	3.42	12	169	1.5	1.6	8.3
0235+164	2003 Mar 1	0.90	0.52	−3	1.62	1.45	72	167	0.8	1.1	7.9
0238−084	2002 Oct 9	3.14	1.79	9	0.62	0.34	<2	...	1.9	1.9	0.1
0300+470	2002 Nov 23	0.81	0.61	−23	1.29	1.04	12	79	0.6	0.8	...
0316+413	2003 Mar 1	0.69	0.55	2	10.64	2.65	45	136	10.0	5.0	0.4
0333+321	2003 Mar 29	0.95	0.51	−12	2.25	1.73	44	48	0.7	1.2	8.4
0336−019	2003 Feb 5	1.32	0.56	−7	3.45	2.72	121	82	1.2	1.9	7.7
0403−132	2002 May 31	1.44	0.53	−8	1.40	1.32	7	21	0.7	1.1	6.5
0415+379	2002 Oct 9	1.44	0.79	3	1.66	1.17	9	98	2.0	1.2	1.0
0420−014	2003 Mar 1	1.14	0.46	−7	10.60	9.46	92	89	5.5	2.8	7.8
0422+004	2002 Jun 15	1.28	0.52	−7	1.78	1.64	137	5	0.8	1.0	...
0430+052	2003 Feb 5	1.20	0.56	−5	2.50	1.04	74	170	1.5	1.5	0.7
0446+112	2002 May 31	1.22	0.56	−8	2.25	2.11	22	166	2.5	1.5	...
0458−020	2003 Mar 1	1.12	0.45	−6	1.14	1.04	13	125	0.8	0.8	8.2
0528+134	2003 Feb 5	1.11	0.56	−6	3.17	2.64	137	123	1.2	0.9	8.3
0529+075	2002 May 31	1.30	0.58	−9	1.36	0.69	3	49	0.7	1.2	...
0529+483	2002 Oct 9	0.88	0.60	−16	1.03	0.90	16	155	0.6	0.8	8.3
0552+398	2003 Mar 29	0.91	0.52	−5	3.67	2.39	56	105	0.7	1.7	8.2
0605−085	2003 Feb 5	1.38	0.53	−6	1.50	1.00	26	145	0.7	1.0	7.7
0607−157	2003 Mar 1	1.24	0.46	−5	4.77	4.04	159	101	2.0	1.5	4.7
0642+449	2003 Mar 29	0.89	0.56	−10	4.31	3.45	136	32	0.7	2.0	7.4
0648−165	2002 Nov 23	1.44	0.51	−9	2.68	2.31	27	76	0.9	1.2	...
0716+714	2003 Aug 28	0.73	0.69	37	2.59	2.52	130	40	0.8	1.2	...
0727−115.......	2003 Mar 1	1.24	0.46	−6	5.31	4.09	165	97	1.3	2.1	8.5
0730+504	2002 Jun 15	0.79	0.58	4	0.86	0.72	6	97	0.5	0.8	7.2
0735+178	2002 Nov 23	1.19	0.57	−8	1.41	0.85	19	117	0.6	0.8	...
0736+017	2003 Mar 1	1.14	0.47	−8	1.79	1.49	6	141	0.9	1.3	3.2
0738+313	2003 Feb 5	1.10	0.71	−32	1.38	0.51	14	61	0.9	1.1	6.8
0742+103	2004 Feb 11	1.43	0.57	−14	1.32	0.59	3	136	0.8	1.0	8.0
0748+126	2003 Feb 5	1.15	0.59	−11	2.13	1.79	69	0	0.7	0.9	7.8
0754+100	2002 Nov 23	1.26	0.56	−7	1.83	1.38	101	20	0.6	0.7	4.1
0804+499	2004 Feb 11	0.77	0.58	−21	0.68	0.61	2	42	0.7	1.0	8.4
0805−077	2002 Jun 15	1.29	0.50	−7	1.58	1.28	8	40	0.9	1.1	8.4
0808+019	2004 Feb 11	1.32	0.52	−8	0.49	0.46	43	179	0.8	1.0	7.9
0814+425	2004 Feb 11	0.83	0.58	−20	0.77	0.67	16	79	0.7	0.9	...
0823+033	2003 Jun 15	1.23	0.52	−7	1.12	0.97	8	20	0.7	1.1	6.1
0827+243	2002 May 31	1.03	0.59	−15	1.99	1.77	13	66	0.7	2.5	7.9
0829+046	2003 Aug 28	1.31	0.59	−7	0.81	0.43	60	48	1.0	1.3	3.0
0836+710	2003 Mar 29	0.85	0.54	12	1.99	1.19	43	95	0.8	1.4	8.3
0851+202	2002 Oct 9	1.17	0.57	−12	4.12	3.48	97	14	1.3	1.5	4.5
0906+015	2003 Mar 29	1.20	0.52	−2	2.43	1.89	110	145	1.2	1.2	8.0
0917+624	2002 Jun 15	0.79	0.63	−79	0.90	0.57	33	32	0.7	1.1	8.4
0923+392	2002 Oct 9	0.91	0.61	−9	8.08	4.31	60	85	3.0	3.5	7.1
0945+408	2002 Oct 9	0.90	0.62	−9	1.59	1.00	7	56	0.6	0.8	8.3
0955+476	2002 Jun 15	0.74	0.60	−49	1.75	1.56	12	156	1.4	1.2	8.4
1036+054	2002 May 31	1.27	0.55	−10	2.66	2.55	37	74	0.9	1.5	...
1038+064	2002 May 31	1.28	0.54	−10	1.49	1.03	7	100	0.7	0.9	8.4
1045−188	2002 Jun 15	1.34	0.49	−7	1.33	1.11	50	64	1.0	1.2	6.7
1055+018	2003 Feb 5	1.28	0.53	−7	3.72	3.15	121	145	2.0	1.5	7.8
1124−186.......	2003 Mar 1	1.21	0.44	−4	1.41	1.30	27	23	0.9	1.1	8.1

1406

TABLE 3—Continued

Source (1)	Epoch (2)	B_{maj} (mas) (3)	B_{min} (mas) (4)	B_{PA} (deg) (5)	I_{tot} (Jy) (6)	I_{peak} (Jy beam^{-1}) (7)	P_{tot} (mJy) (8)	EVPA$_{tot}$ (deg) (9)	I_{base} (mJy beam^{-1}) (10)	P_{base} (mJy beam^{-1}) (11)	Scale (pc mas^{-1}) (12)
1127−145.......	2002 Oct 9	1.55	0.52	−8	2.56	1.07	121	140	2.0	2.0	8.3
1150+812	2002 Jun 15	0.69	0.56	−78	1.51	0.98	30	32	0.8	1.2	8.3
1156+295	2002 Nov 23	0.99	0.57	−14	2.12	1.86	41	145	0.7	0.9	7.3
1213−172	2002 Jun 15	1.27	0.46	−7	1.68	1.11	50	171	0.7	1.2	. . .
1219+044	2002 Jun 15	1.20	0.49	−9	0.94	0.91	2	4	0.8	1.1	7.9
1222+216	2002 May 31	1.08	0.57	−12	0.82	0.56	51	158	0.7	0.9	5.6
1226+023	2002 Oct 9	1.66	0.55	−14	22.78	8.91	345	146	16.0	18.0	2.7
1228+126	2003 Feb 5	1.23	0.55	−9	2.74	1.28	5	135	0.7	1.0	0.1
1253−055	2002 Nov 23	1.44	0.52	−9	16.37	10.31	1244	52	5.0	7.0	6.3
1308+326	2003 Mar 29	0.93	0.56	1	2.99	2.48	87	119	0.7	1.5	8.0
1324+224	2002 Oct 9	1.26	0.58	−15	0.62	0.55	8	128	0.4	0.9	8.4
1334−127	2003 Mar 1	1.21	0.45	−5	5.05	4.31	78	165	2.0	3.0	6.3
1413+135	2002 Nov 23	1.21	0.58	−12	1.03	0.88	1	107	0.6	0.9	3.9
1417+385	2002 Jun 15	0.90	0.51	−21	0.90	0.84	19	148	0.8	1.0	8.4
1458+718	2003 Aug 28	0.81	0.64	−26	1.29	0.57	51	74	0.9	1.4	7.8
1502+106	2003 Mar 29	1.14	0.54	0	1.95	1.45	15	109	1.3	1.2	8.4
1504−166	2003 Feb 5	1.40	0.52	−5	1.60	0.93	18	68	1.7	1.3	7.7
1510−089	2002 Nov 23	1.50	0.51	−10	2.93	2.73	106	27	1.6	1.1	5.0
1538+149	2004 Feb 11	1.56	0.55	−19	1.18	0.97	129	140	0.7	1.0	6.7
1546+027	2003 Mar 29	1.20	0.51	−2	1.70	1.42	31	46	1.0	1.0	5.5
1548+056	2003 Mar 1	1.07	0.49	−5	2.93	1.66	88	100	1.0	1.5	8.4
1606+106	2002 Nov 23	1.25	0.59	−13	1.88	1.48	32	125	1.1	1.0	8.3
1611+343	2003 Feb 5	0.96	0.54	−9	4.07	2.72	96	15	1.0	1.1	8.4
1633+382	2003 Mar 29	0.95	0.54	4	4.29	3.48	47	156	0.7	1.0	8.4
1637+574	2002 May 31	0.78	0.62	−8	1.88	1.65	35	127	0.6	0.7	7.3
1638+398	2003 Mar 1	0.78	0.50	−6	0.88	0.68	51	168	0.8	1.0	8.5
1641+399	2002 Nov 23	0.86	0.60	−16	7.25	2.95	151	129	0.9	1.6	6.7
1655+077	2002 Oct 9	1.37	0.54	−9	1.09	0.86	36	130	0.9	1.6	6.8
1726+455	2002 May 31	0.82	0.66	−7	2.18	2.07	81	148	0.7	0.9	7.2
1730−130	2002 Oct 9	1.51	0.54	−7	5.66	4.75	30	71	2.2	5.3	7.8
1739+522	2003 Mar 29	0.87	0.57	18	1.40	1.30	36	166	1.1	1.1	8.4
1741−038	2003 Mar 1	1.17	0.47	−6	7.01	5.95	41	119	4.0	2.6	8.1
1749+096	2002 May 31	1.27	0.56	−11	3.42	3.13	67	177	1.9	1.2	4.7
1751+288	2002 Jun 15	1.01	0.49	−13	1.88	1.84	13	156	0.7	1.0	. . .
1758+388	2003 May 9	0.87	0.60	−11	1.38	1.26	21	33	0.6	0.8	8.3
1800+440	2003 Mar 29	0.89	0.51	14	1.21	1.10	11	53	0.6	1.2	7.0
1803+784	2003 Feb 5	0.67	0.65	47	1.92	1.33	83	100	0.7	0.9	7.1
1823+568	2003 May 9	0.75	0.62	−9	1.59	1.32	124	30	0.6	2.2	7.0
1828+487	2003 Mar 29	0.79	0.61	5	1.89	1.28	35	57	0.9	1.5	7.1
1849+670	2003 Jun 15	0.72	0.65	43	1.74	1.59	53	29	0.8	1.0	7.0
1928+738	2002 Jun 15	0.71	0.54	−58	3.93	2.47	34	79	0.9	1.7	4.5
1936−155	2002 May 31	1.49	0.52	−8	0.83	0.73	14	129	0.7	0.7	8.5
1957+405	2002 Nov 23	0.98	0.62	−38	1.53	0.64	3	146	1.1	1.1	1.1
1958−179	2002 May 31	1.50	0.52	−8	1.06	0.95	8	84	0.7	0.9	6.9
2005+403	2003 Mar 1	0.77	0.52	1	2.82	1.56	67	134	0.9	1.1	8.5
2008−159	2003 Jun 15	1.52	0.53	−7	2.14	1.96	3	128	0.8	1.0	8.3
2021+317	2003 Feb 5	1.07	0.58	−5	0.60	0.39	13	39	0.6	1.1	. . .
2021+614	2003 Mar 1	0.62	0.55	−8	2.26	0.99	<1	. . .	0.9	1.1	3.6
2037+511	2002 Oct 9	0.82	0.62	−11	2.33	1.62	31	75	0.7	1.4	8.5
2121+053	2003 Mar 29	1.16	0.52	−4	2.57	2.13	138	1	1.0	1.7	8.4
2128−123	2003 May 9	1.39	0.51	−6	3.17	1.78	64	113	2.0	4.0	6.1
2131−021	2003 May 9	1.35	0.54	−8	2.21	1.14	52	92	1.0	1.0	8.4
2134+004	2002 May 31	1.37	0.53	−10	6.14	1.62	179	15	3.2	1.9	8.4
2136+141	2002 Nov 23	1.25	0.55	−16	2.75	2.15	89	127	1.0	0.9	8.1
2145+067	2003 Mar 1	1.01	0.44	−4	8.89	5.86	184	35	1.8	2.3	8.0
2155−152	2003 Mar 29	1.21	0.48	−4	2.11	1.27	71	57	2.5	3.0	7.0
2200+420	2002 Jun 15	0.84	0.55	−17	2.16	1.25	176	27	0.8	1.3	1.3
2201+171	2003 Jun 15	1.07	0.56	−6	2.01	1.83	35	170	0.7	1.0	8.1
2201+315	2002 Nov 23	1.04	0.55	−12	3.07	2.23	55	45	1.2	0.9	4.4
2209+236	2003 Mar 1	0.88	0.48	−1	0.85	0.62	81	35	0.8	1.1	8.2
2216−038	2002 May 31	1.41	0.54	−9	2.54	1.95	41	112	1.2	0.9	7.8
2223−052	2002 Oct 9	1.56	0.57	−10	5.17	3.72	158	149	2.6	2.2	8.4
2227−088	2003 Mar 29	1.28	0.50	−4	2.00	1.88	9	30	0.9	1.4	8.5
2230+114	2002 Oct 9	1.31	0.61	−13	3.54	2.32	42	91	2.0	2.4	8.1

TABLE 3—*Continued*

Source (1)	Epoch (2)	B_{maj} (mas) (3)	B_{min} (mas) (4)	B_{PA} (deg) (5)	I_{tot} (Jy) (6)	I_{peak} (Jy beam^{-1}) (7)	P_{tot} (mJy) (8)	EVPA$_{tot}$ (deg) (9)	I_{base} (mJy beam^{-1}) (10)	P_{base} (mJy beam^{-1}) (11)	Scale (pc mas^{-1}) (12)
2243−123	2002 Oct 9	1.60	0.56	−10	1.70	1.03	19	5	1.6	1.0	6.8
2251+158	2003 Mar 29	1.06	0.53	−9	9.64	3.24	127	178	2.7	6.5	7.7
2331+073	2002 Jun 15	1.21	0.51	−9	1.24	0.96	45	142	0.8	1.0	. . .
2345−166	2002 Oct 9	1.74	0.57	−10	1.91	1.39	10	67	0.7	1.0	6.6
2351+456	2002 May 31	0.87	0.57	−16	1.80	1.39	38	27	0.8	1.4	8.4

Notes.—Columns are as follows: (1) IAU name (B1950.0); (2) date of VLBA observation; (3) FWHM major axis of restoring beam; (4) FWHM minor axis of restoring beam; (5) position angle of major axis of restoring beam; (6) total I flux density; (7) peak flux density in the image; (8) total linearly polarized flux density; (9) integrated electric vector position angle; (10) lowest I contour in image; (11) lowest P contour in image; (12) linear scale. Table 3 is also available in machine-readable form in the electronic edition of the *Astronomical Journal*.

calibrated visibility data using natural weighting and a cell size of 0.1 mas pixel^{-1}. The best-fit elliptical Gaussian restoring beam's FWHM dimensions varied between 0.45 and 1.5 mas, depending on the declination of the source. The restoring beam parameters are listed in columns (3)–(5) in Table 3. The typical rms noise level, obtained by examining pixels well away from the source in each Stokes I image, was ~0.2 mJy beam^{-1}. Based on comparisons of highly compact sources to near-simultaneous UMRAO observations, we estimate that the absolute flux density scaling of our VLBA observations is accurate to within 5%.

In Figure 1 we display the first-epoch 15 GHz VLBA images of the entire MOJAVE sample. Each panel contains two images of the same source, the first consisting of I contours with linear fractional polarization overlaid in color. The latter is defined as P/I, where $P = (Q^2 + U^2)^{1/2}$. The second image shows the single lowest I contour plus contours of polarized intensity, as well as tick marks indicating the electric polarization vector directions. In most cases the lowest contour levels correspond to 3 and 5 times the rms in I and P, respectively. The linear scale factor of each image in parsecs per milliarcsecond is given in column (12) of Table 3 for those sources with a known redshift.

In columns (6) and (8) of Table 3 we list the total 15 GHz VLBA I and P flux densities of each source, respectively. These are determined using the sums of I, Q, and U intensities of all of the pixels shown in Figure 1 whose I intensities exceeded 3 times the rms noise level of the I image. Using Rayleigh statistics, the noise in the P image was estimated to be 0.66 times the average of the Q and U rms noise levels. If the total P did not exceed 5 times this value, the latter was used as an upper limit in column (8). The integrated EVPA listed in column (9) is calculated using the total Q and U flux densities of the source, where EVPA = (1/2) arctan (U/Q).

3.3. *Visibility Model Fitting*

From observations of jet phenomena associated with young and evolved stars in our Galaxy, as well as nearby AGN jets such as those in M87 and Centaurus A, it is known that these outflows have highly complex three-dimensional structures that do not easily lend themselves to simple statistical analysis. However, the vast majority of AGNs lie at cosmological distances, and many of these details are blurred out by the limited spatial resolution of current ground-based radio interferometers. A close examination of the images in Figure 1 shows several instances (e.g., 0007+106, 0446+112, 0642+449, 1751+288) in which no actual jets are evident, since they lie below the resolution and/or sensitivity level of the VLBA at this frequency. At the other extreme, there are also cases in which the jet is clearly resolved in a transverse direction (e.g., 0836+710, 1641+399, 1828+487),

making a more detailed analysis possible. For the statistical purposes of this paper, we have fit each source with a minimum number of elliptical Gaussian "components" that, when convolved with the restoring beam, generally reproduce the observed structure. In a separate paper we will present a more detailed ridge line–based analysis of approximately one-third of the sample members whose jets are not fully described by multiple Gaussian fits.

We carried out our analysis in the (u, v)-plane by fitting the brightest features in each source with two-dimensional Gaussian components. Using the *modelfit* task in DIFMAP, we fit several components to each source, resorting to zero-size (delta function) points if the least-squares routine shrank the fitted Gaussian minor axis to extremely small values. These fits provided positions, sizes, and flux densities for the brightest, most compact jet features, which are tabulated in Tables 4 and 5. Based on our previous 15 GHz studies (see Appendix A of Homan et al. 2002), we estimate typical errors of 5% on the total intensities and positional errors of ~1/5 of the restoring beam dimension. For the brightest components, the errors are smaller by approximately a factor of 2.

The milliarcsecond morphology of most sources consists of a strong, flat-spectrum "core" component that is typically unresolved along one or both axes of the restoring beam and is located at the extreme end of a more diffuse jet structure. This core component is usually the brightest feature in the image and is generally thought to represent the region near the base of the jet where it becomes optically thick. Observational evidence of apparent core shifts with frequency (e.g., Lobanov 1998) support this view.

3.3.1. *Core Measurements*

We list the position of the fitted core component in polar coordinates with respect to the map center in columns (2) and (3) of Table 4. In most cases the core offset is negligible (less than one pixel, or 0.1 mas), since the phase self-calibration process tends to shift the map center to lie on the brightest feature in the source. Nonzero offsets occur when a strong jet feature lies very close to the core (e.g., 0224+671) or when the source is dominated by an exceptionally strong jet feature downstream (e.g., 0923+392). In other cases, there is the possibility that we are seeing both the jet and the counterjet. In blazars the latter is not usually visible, since its radiation is beamed away from us. There are four sources in our sample in which counterjets have been detected in other studies: 0316+413 (3C 84), 0238−084 (NGC 1052), 1413+135, and 1957+405 (Cygnus A). The exact location of the core in these sources is not well defined because of possible foreground absorption in the vicinity of the central

TABLE 4
Core Component and Integrated Jet Properties

Source (1)	r (mas) (2)	Core P.A. (deg) (3)	I_{core} (4)	Maj. (mas) (5)	Ratio (6)	Maj. P.A. (deg) (7)	$\log T_{b,core}$ (K) (8)	m_{core} (%) (9)	EVPA$_{core}$ (deg) (10)	m_{jet} (%) (11)
0003−066	...	...	2.47	0.93	0.26	1	10.8	4.3	195	3.5
0007+106	...	...	0.94	...	...	...	>12.9	<0.06	...	<14.6
0016+731	...	...	1.03	0.13	0.60	289	11.7	1.0	112	<7.4
0048−097	...	...	0.73	0.21	0.34	12	11.4	4.2	209	<17.0
0059+581	...	...	3.25	0.13	0.85	8	12.1	2.0	191	<5.9
0106+013	...	...	1.84	0.28	0.39	3	11.5	1.5	185	2.4
0109+224	...	...	0.86	...	...	...	>12.9	4.6	87	4.8
0119+115............	...	...	0.90	0.30	0.13	26	11.6	5.6	0	5.9
0133+476	...	...	4.22	0.12	0.23	296	12.8	3.1	296	0.4

Notes.—Columns are as follows: (1) IAU name (B1950.0); (2) core position offset from the map center; (3) core position angle with respect to the map center; (4) fitted Gaussian core flux density; (5) FWHM major axis of the fitted core Gaussian; (6) axial ratio of the fitted core Gaussian; (7) major axis position angle of the fitted core Gaussian; (8) log of the core brightness temperature in kelvins; (9) fractional polarization at the core position; (10) electric vector position angle at the core position; (11) integrated fractional polarization of the jet. Table 4 is published in its entirety in the electronic edition of the *Astronomical Journal*. A portion is shown here for guidance regarding its form and content.

nucleus. In such cases we have considered the feature closest to the map center to be the core. Other sources in our sample that may have visible counterjets are 0742+103, 1548+056, and 2021+614. Multifrequency imaging of these AGNs would aid in identifying the core based on its predicted flat spectral index, variability, and high brightness temperature. Such a study of 2021+614 is currently underway (M. Lister et al. 2005, in preparation).

The fitted flux density and Gaussian parameters of the core components are given in columns (4)–(7) of Table 4. The bright-

ness temperatures in column (8) are calculated in the observer's frame assuming a Gaussian profile using the formula

$$T_b = \frac{(1.221 \times 10^{12}) S_{core}}{\nu_{obs}^2 a_{maj} a_{min}} \text{ K},$$

where S_{core} is the core flux density in janskys, ν_{obs} is the observing frequency in GHz, and a_{maj} and a_{min} are the FWHM major and minor axes of the fitted core Gaussian, respectively, in milliarcseconds. It should be noted that these are best-fit

TABLE 5
Jet Component Properties

Source (1)	r (mas) (2)	P.A. (deg) (3)	Maj. (mas) (4)	Ratio (5)	Maj. P.A. (deg) (6)	I (mJy) (7)	m (%) (8)	EVPA (deg) (9)
0003−066	0.89	260	...	...	...	79	11.1	42
	1.96	304	...	...	...	58	18.8	16
	6.63	281	1.61	0.62	359	216	11.6	97
0007+106	0.09	274	...	...	...	439	<0.06	...
0016+731	1.24	136	1.27	0.58	310	36	<14.5	...
0048−097	1.25	359	...	...	...	9	4.7	208
0059+581	1.43	235	2.63	0.27	72	39	<20.4	...
0106+013	0.30	235	...	...	...	506	2.6	201
	0.57	243	1.18	0.49	57	456	2.1	213
	2.96	239	2.54	0.45	9	48	<30.3	...
0109+224	0.24	92	...	...	...	108	4.3	91
	1.94	87	2.44	0.26	85	38	13.4	230
0119+115........................	0.55	10	...	...	...	98	6.6	357
	1.65	359	0.57	0.61	347	181	7.0	281
	2.44	11	0.92	0.61	11	64	8.7	246
0133+476	0.57	331	0.91	0.25	335	194	2.4	300
	2.06	325	2.15	0.42	347	65	<20.8	...
0202+149	0.62	338	0.35	0.20	330	1114	0.08	257
	0.77	320	...	...	...	110	<0.1	...
	1.21	279	...	...	...	12	<6.5	...
	3.16	297	1.81	0.69	279	59	<6.1	...
	5.19	302	0.95	0.27	40	34	<3.4	...
	5.35	317	2.50	0.52	44	91	<5.2	...

Notes.—Columns are as follows: (1) IAU name (B1950.0); (2) distance from the fitted core position; (3) position angle of the component with respect to core position; (4) major axis of the fitted Gaussian; (5) axial ratio of the fitted Gaussian; (6) position angle of the major axis of the fitted Gaussian; (7) fitted component flux density; (8) fractional polarization at the component position; (9) electric vector position angle at the component position. Table 5 is published in its entirety in the electronic edition of the *Astronomical Journal*. A portion is shown here for guidance regarding its form and content.

brightness temperatures and in many cases may in fact be lower limits because of the limited spatial resolution of the data. For those cores that were completely unresolved along at least one axis of the restoring beam (such that the best fit was a delta function), a lower limit on T_b was calculated assuming a minimal resolvable component size. The expression for the latter, based on the signal-to-noise ratio at the core position and the restoring beam dimensions, is given by Kovalev et al. (2005).

Columns (9) and (10) list the fractional polarization and EVPA of the core, which are calculated from the mean I, Q, and U of the nine contiguous pixels centered at the fitted core position. In cases in which the polarization is below the lowest P contour level listed in column (11) of Table 3, upper limits are given corresponding to five times the P rms noise level.

3.3.2. Jet Measurements

We use the same Gaussian component method to describe the jet emission in the MOJAVE sample. The results of these fits are given in Table 5. Additionally, we measure the mean jet polarization by integrating over all jet emission. This is determined in the image plane using only those pixels that are above the base I contour level listed in Table 3. We exclude pixels in the core region defined as

$$\left(\frac{x}{b_{\mathrm{min}}}\right)^2 + \left(\frac{y}{b_{\mathrm{maj}}}\right)^2 \leq \frac{\ln|I_{\mathrm{core}}/I_{\mathrm{base}}|}{4\ln 2},$$

where b_{maj} and b_{min} are the FWHM major and minor axes of the Gaussian restoring beam, respectively, and x and y are the right ascension and declination coordinates of the pixel with respect to the core. The term I_{base} is the lowest contour level in the image, and I_{core} is the pixel intensity at the core position. Outside this region, the emission from the core is below the lowest contour level. For most sources, it corresponds to an ellipse with dimensions approximately equal to those of the Gaussian restoring beam listed in Table 3.

4. DISCUSSION

4.1. Core Component Properties

Although the flat-spectrum core components are responsible for much of the polarized and total flux density in our VLBA images, their properties are the most difficult to interpret because they likely represent a blend of many small individual emitting regions close to the base of the jet. In roughly one-third of the sources, the core feature could be adequately fitted by an unresolved point model, yielding only a lower limit on the brightness temperature. The observed brightness temperatures of the remaining sources are typically above 10^{11} K, which is close to the detection limit of ground-based interferometers for cores with flux densities of a few hundred millijanskys. For this reason we expect that many of the T_b values listed in Table 4 are also lower limits. Indeed, a full (u, v) plane analysis of the fine-scale structure of 250 flat-spectrum AGNs in the MOJAVE and 2 cm Survey samples by Kovalev et al. (2005) shows that in over 65% of the sources, at least half of the total flux density is unresolved on the longest VLBA baselines.

The relative prominence of the core component with respect to the remainder of the VLBI jet varies significantly among the sources in our sample. We define the core-to-jet flux density ratio as

$$R_j = \frac{S_{\mathrm{core}}}{S_{\mathrm{jet}}(1+z)^{0.7}},$$
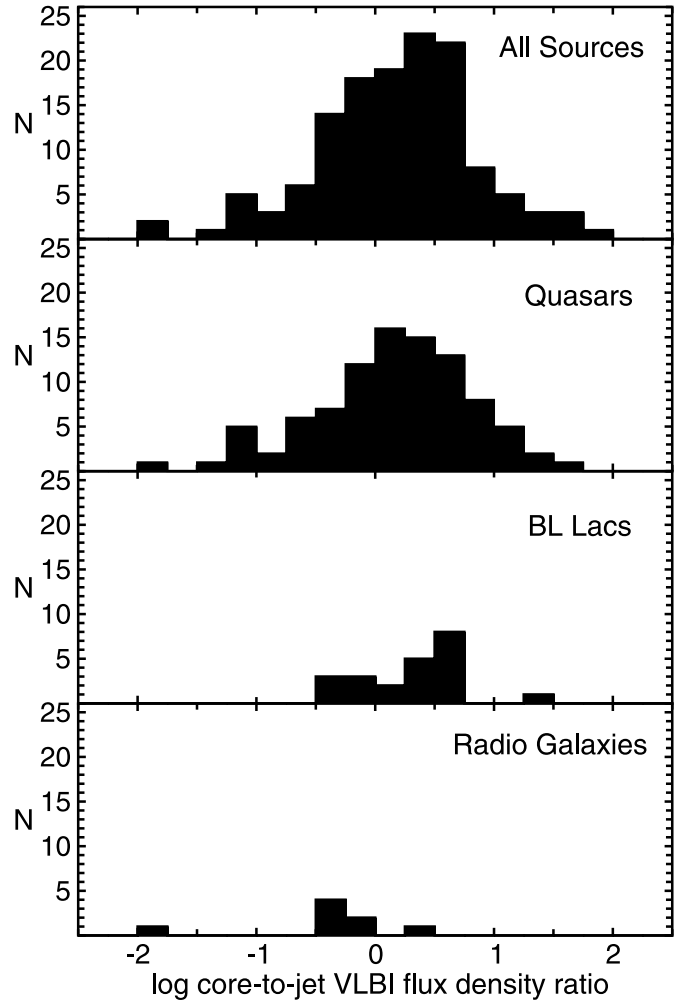
Fig. 2.—Distribution of the VLBI core-to-jet ratio (R_j) for the full MOJAVE sample (*top panel*) and major optical subclasses (*bottom panels*).

where we have assumed typical spectral indices of 0 and -0.7 for the core and jet, respectively. For sources without measured redshifts we assume a typical value of $z = 1$. The distribution of R_j (Fig. 2) is very broad, spanning 4 orders of magnitude, with a peak at approximately $R_j = 3$. The spread in R_j is likely a result of strong flux variability in the core components, as well as a wide range of Doppler factors in the jet population. The latter broadens the distribution, since the core and jet emission, having different spectral indices, are expected to be beamed by different amounts. We do not find R_j to be correlated with either redshift or angular size distance according to Kendall's τ tests.

The core components have typically low fractional polarizations ($m_{\mathrm{core}} \lesssim 5\%$) and range up to a maximum of $\sim 10\%$ in the case of $1538 + 149$ (Fig. 3). No polarized emission was detected in any of the eight radio galaxy cores. This was also the case for seven quasars and one BL Lac object ($1413+135$). As we discuss in § 4.2, the fractional polarization levels are generally much higher in jet regions downstream from the core.

The linearly polarized emission may be strongly depolarized in the core regions, either from an external screen or internal plasma processes. This would also imply a random rotation of the observed electric vectors with respect to the jet; however, this is not the case for the BL Lac cores (Fig. 4). The latter tend to have core electric vectors that are within $20°$ of the inner jet direction. Faraday depolarization without accompanying rotation
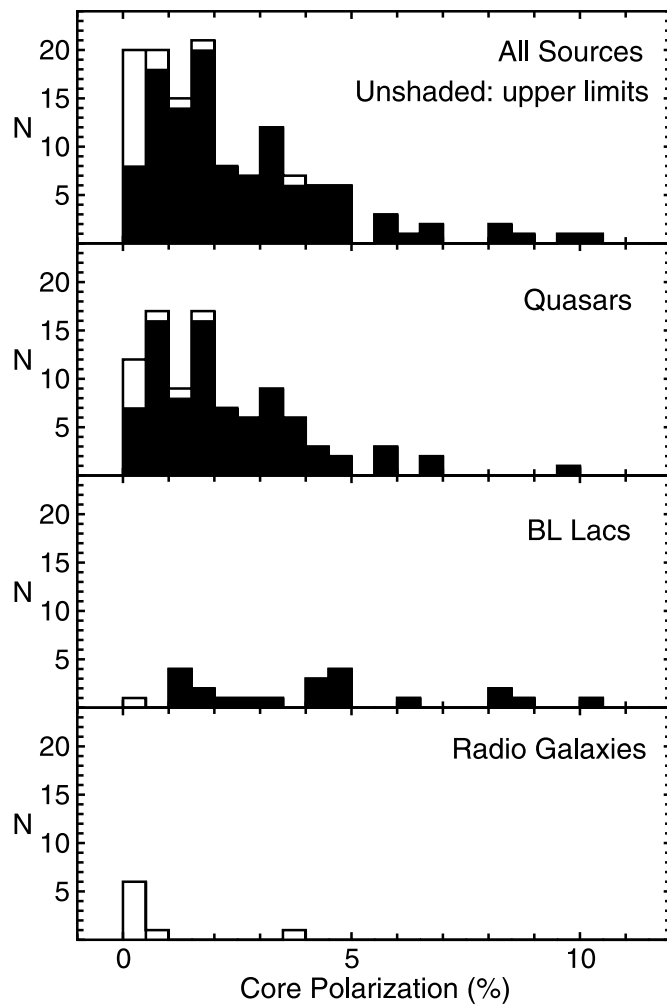
Fig. 3.—Linear fractional polarization of the VLBI core component for the entire MOJAVE sample (*top panel*) and three major optical subclasses (*bottom panels*). The unshaded boxes represent upper limits on those cores in which no linear polarization was detected. The distribution for the BL Lac objects differs from the quasars at 99.9% confidence according to a Wilcoxon test.

Fig. 4.—Distribution of the electric vector offsets with respect to inner jet direction at the locations of VLBI cores in the MOJAVE sample. The inner jet direction is defined as the position angle of the Gaussian jet component closest to the core. The BL Lac and quasar distributions differ at the 99.9% confidence level according to a K-S test.

is possible but typically requires special geometries that include a mixture of Faraday thin and thick material on scales smaller than the restoring beam. Some quasars are known to have large parsec-scale rotation measures (Zavala & Taylor 2004), but there are currently not enough data to indicate whether there are strong differences in the Faraday screens of weak- and strong-lined blazars. If such differences do exist, they must persist out to several hundred parsecs from the central engine, since we show in § 4.3.2 that these polarization differences are also present in jet regions well downstream from the cores.

The case for Faraday depolarization is much stronger in the seven sources in our sample for which very little or no polarized emission is present in our images. The jets of the radio galaxies 0007+106, NGC 1052, M87, Cygnus A, and 2021+614 lie at larger viewing angles and are heavily depolarized by material associated with an obscuring torus located in their host galaxies. Detailed VLBI studies of several powerful radio galaxies by Middelberg (2004) support this picture. The two remaining unpolarized sources in our sample, the BL Lac object 1413+135 (Perlman et al. 2002) and the peaked-spectrum quasar 0742+103 (Best et al. 2003), also display heavy absorption features in their central regions. The nearby radio galaxy 3C 84 also suffers from heavy foreground absorption (Walker et al. 2000), and we detect

polarized emission only in the southern lobe, which is presumably located closer to us (Fig. 1).

Apart from possible Faraday depolarization, the cores may appear weakly polarized because of optical depth effects. Synchrotron radiation from an optically thick region such as the core will tend to be weakly polarized, because the fields are usually not well ordered over the short path length into the plasma (e.g., Hughes 2005). Also, if the core region contains regions of orthogonal electric vectors, these can combine within the VLBI restoring beam to lower the net polarization. We find a tendency for the most unresolved cores (those with only lower limits on brightness temperature) to have electric vectors that are better aligned with the inner jet direction (Fig. 5). Such an alignment might be expected, for example, from a strong standing shock near the base of the jet. The misaligned cases may simply be instances in which we have insufficient spatial resolution to separate one or more components close to the base of the jet. Since such features will eventually propagate downstream, it will be possible to investigate this scenario more fully using the full multi-epoch MOJAVE polarization data set.

4.2. Jet Properties

At least 94% of the MOJAVE sources have one-sided jet morphologies, which is a strong reflection of the sample-selection biases. If the milliarcsecond-scale emission from these jets is highly anisotropic (i.e., beamed along the flow direction), the sources with the highest flux densities will tend to have their jet axes preferentially aligned toward the observer. Emission from the receding jet will be beamed in the opposite direction, rendering it nearly undetectable. This tendency toward one-sided jets is well known from previous VLBI surveys (see the review by Urry & Padovani 1995) and is considered to be key evidence for relativistic bulk motion in AGN jets.

There are still two ways that lesser aligned jets (lying closer to the plane of the sky) can meet the MOJAVE selection criteria
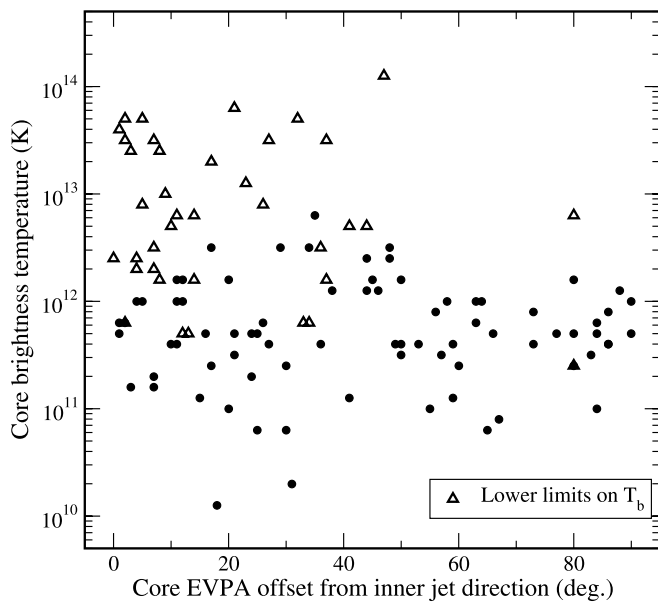
Fig. 5.—Observed brightness temperature vs. electric vector misalignment angle for core components in the MOJAVE sample. The filled circles denote best-fit brightness temperatures, and the open triangles denote lower limits. Cores with the highest brightness temperatures tend to have electric vectors that are better aligned with the inner jet direction.

and yet appear as two-sided. They may have (1) sufficient flux density merely because of their proximity (e.g., NGC 1052, Cygnus A, 3C 84) or (2) sufficiently small intrinsic size that their (isotropic) lobe emission dominates their milliarcsecond-scale flux. Some of the peaked-spectrum radio sources, believed to be young jets, fall into this category. Possible examples in MOJAVE include 0742+103 and 2021+614.

Despite the large amount of foreshortening caused by the orientation bias of the MOJAVE sample, we still find several major trends in the observed jet properties. In Figure 6 we plot the linear fractional polarization of fitted jet components against
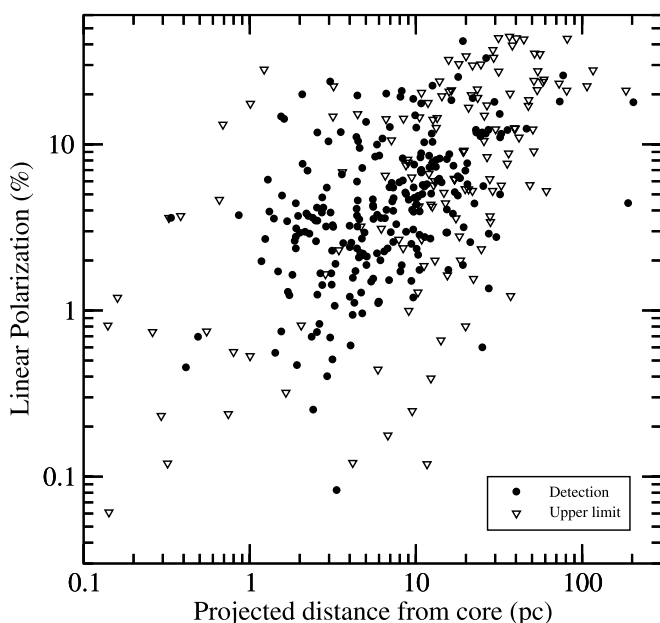
Fig. 6.—Linear fractional polarization of individual jet components vs. projected distance from the VLBI core component. The filled circles indicate polarization detections, while the open triangles represent upper limits.
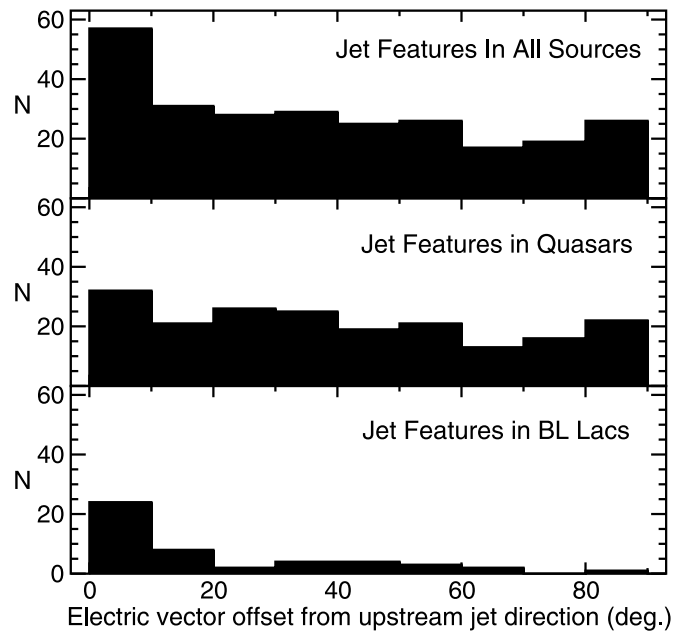
Fig. 7.—Distribution of the electric vector offsets with respect to the upstream jet direction at the locations of jet components in the full MOJAVE sample (*top panel*) and for optical subclasses (*bottom panels*). The upstream jet direction is defined as the position angle to the nearest component located closer to the core. The BL Lac and quasar distributions differ at greater than 99.99% confidence according to a Wilcoxon test.

their projected distance from the core in parsecs. Ignoring the artificial trend of the upper limits getting larger with distance (because of the weakening flux density of the jet components), there is a clear upward trend of fractional polarization. These selection effects do not affect the upper left corner of this diagram, and a survival analysis test that takes into account the upper limits confirms a trend at greater than 99.99% confidence. This increase in polarization with distance downstream has also been seen in smaller samples at 5 GHz (Cawthorne et al. 1993), 15 GHz (Homan et al. 2002), 22 GHz (Lister & Smith 2000), and 43 GHz (Lister 2001). The polarizations at the sites of the fitted Gaussians range up to a maximum of $\sim$40% seen in 3C 279 (1253$-$055), with more typical values of $\sim$5%. However, in many jets the maximum in fractional polarization does not occur at the locations of fitted components, with some regions being more than 50% linearly polarized (Fig. 1). Such high values indicate extremely well-ordered fields in optically thin synchrotron-emitting regions and can potentially be used to constrain the viewing angle to the jet (e.g., Cawthorne & Wardle 1988).

The EVPA orientations of the jet components lie at a variety of angles to the local jet direction, which we define as the direction to the nearest component upstream (Fig. 7). The distribution of EVPA offsets is peaked at $0°$, indicating an excess of jet components with electric vectors aligned with the jet. Assuming that the jet components are optically thin and that the magnetic field lies perpendicular to the observed electric field vectors, the form of the distribution is similar to that predicted for an ensemble of oblique shocks with random orientations within the jet (Lister et al. 1998). Transverse shocks aligned with the flow always have EVPA offsets of zero, regardless of observer viewing angle (Cawthorne & Cobb 1990), so these cannot be dominant in quasar jets. There is no overall trend between the EVPA offset and projected distance from the core as seen by Lister & Smith (2000) at 43 GHz. Our observations are probing
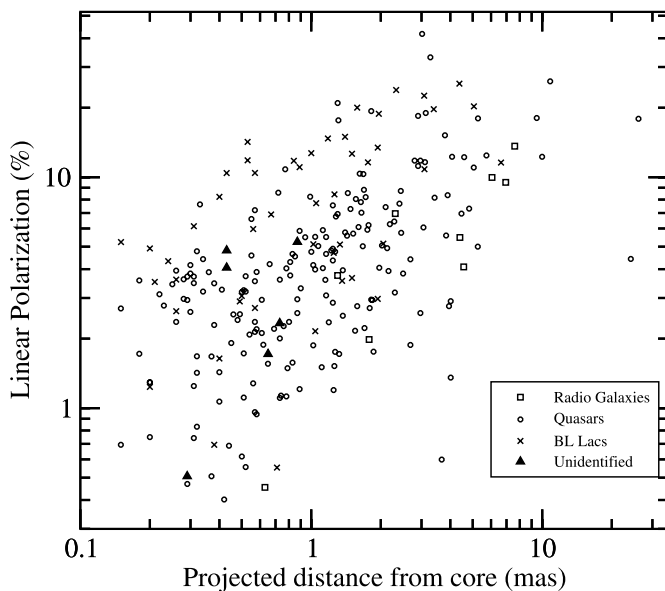
Fig. 8.—Linear fractional polarization of individual polarized jet components vs. projected angular distance from the VLBI core component. The open circles and squares denote those associated with quasars and radio galaxies, respectively, while the crosses denote those associated with BL Lac objects. The filled triangles belong to jets with no known optical counterparts. [*See the electronic edition of the Journal for a color version of this figure.*]

regions much farther downstream at poorer spatial resolution, however, and the steep falloff in jet intensity typically prevents polarized emission from being detected in the outermost components.

4.3. *Connections with Optical Emission Line Properties*

There are now several studies (Cawthorne et al. 1993; Lister et al. 1998; Lister 2001) that have found substantial differences in the parsec-scale polarization properties of weak- versus strong-lined blazars. These AGN classes are commonly referred to as high-polarization radio quasars (HPRQ) and BL Lac objects, respectively, with the division occurring at a rest-frame equivalent emission-line width of 5 Å. This number is somewhat arbitrary, since historically there has been little evidence for any bimodality in the emission line width distribution of radio-loud AGNs, although Landt et al. (2004) have proposed a new classification scheme based on a bimodality of O [III] line width. Furthermore, the duty cycles of emission-line variability are not well known, making the BL Lac classification of individual objects often controversial.

Given these caveats, we use the most prevalent BL Lac and quasar classifications found in the literature (see Table 1) to re-examine the possible differences in the parsec-scale jets of these two optical classes using a large, complete blazar sample. For quantities that do not involve limits, we use the Kolmogorov-Smirnov (K-S) test, and for censored quantities we use Gehan's generalized Wilcoxon test from the ASURV survival analysis package (Lavalley et al. 1992).

4.3.1. *Core Component Properties*

We find the VLBI core components of BL Lac objects to be typically more polarized than the quasars (Fig. 3). They also have electric vectors (E-vectors) preferentially aligned with the inner jet direction, whereas the quasar cores show no preferred E-vector orientation (Fig. 4). Although the median core-to-jet ratio for BL Lac objects appears to be slightly higher than for
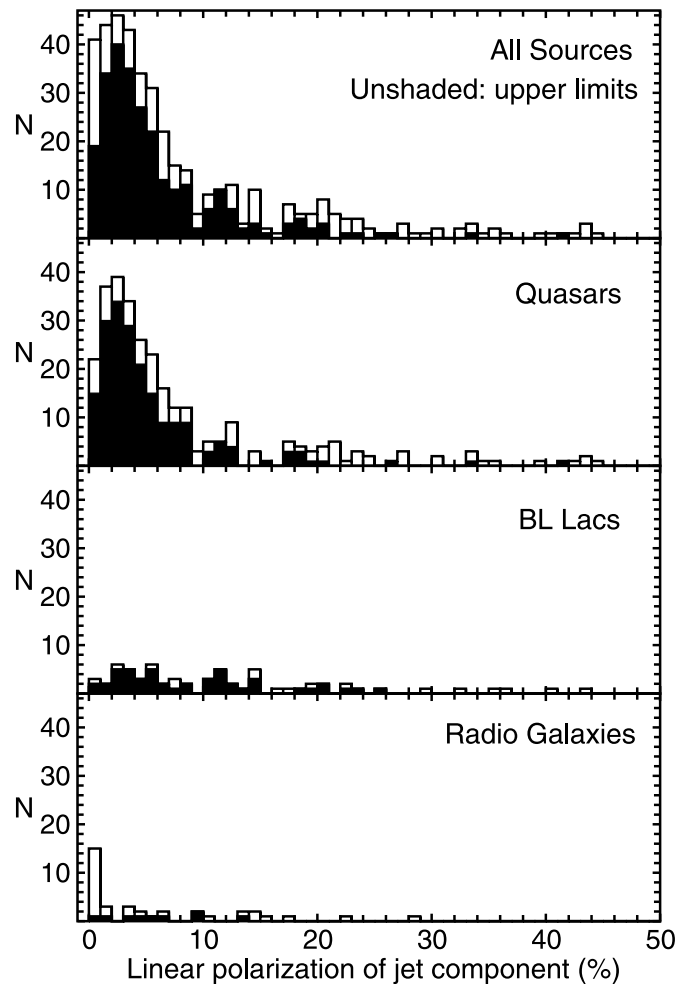
Fig. 9.—Distributions of the linear fractional polarization of jet components in the full MOJAVE sample (*top panel*) and optical subclasses (*bottom panels*). The unshaded boxes represent upper limits for those components with no detected polarization. The quasar and BL Lac distributions differ at greater than 99.99% confidence according to a Wilcoxon test.

quasars (Fig. 2), the K-S test only gives a 89% probability that the two are drawn from different parent distributions.

4.3.2. *Jet Properties*

Lister (2001) found that at 43 GHz, the jets of BL Lac objects in the Pearson-Readhead sample tend to be more polarized at a given projected distance from the core than those of quasars. We confirm these findings using the much larger MOJAVE sample at 15 GHz. At our lower observing frequency, it is possible to image much more of the faint, steep-spectrum regions located farther down the jet, at the expense of poorer spatial resolution. In Figure 8 we plot fractional polarization versus projected angular distance from the core for all jet components in the MOJAVE sample with detected polarized emission. Although the BL Lac jet components are spread over a large region of the diagram, most lie near the top of the distribution, as also seen at 43 GHz by Lister (2001). The jet components of BL Lac objects are not only more polarized than quasars (Fig. 9) but also have electric vectors preferentially aligned with the ridge line (Fig. 7).

4.3.3. *Possible Luminosity and Redshift Biases*

One possible explanation for the polarization differences in quasars and BL Lac objects is that the latter are preferentially
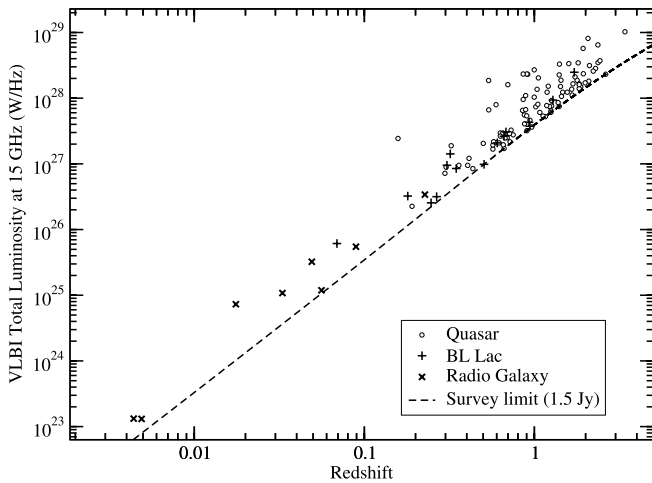
FIG. 10.—Maximum 15 GHz total VLBA luminosity vs. redshift for optically identified MOJAVE sources. The dashed line corresponds to the survey limit of 1.5 Jy for northern sources, assuming flat radio spectra. The open circles denote quasars, the plus symbols denote BL Lac objects, and the crosses represent radio galaxies. [*See the electronic edition of the Journal for a color version of this figure.*]

located at lower redshifts and therefore have lower luminosities in our flux-limited sample. In Figure 10 we show a plot of maximum total 15 GHz VLBA luminosity versus redshift for the optically identified objects in the MOJAVE sample. These luminosities are calculated according to $L = 4\pi D_l^2 S_{15}(1 + z)^{-1}$, where D_l is the luminosity distance and S_{15} is the 15 GHz VLBA flux density. K-S tests indicate that the BL Lac objects are concentrated in a different region of the L-z plane than the quasars.

As a check on possible biases in our analysis, we reperformed our statistical tests on subsamples that included only those BL Lac objects and quasars with maximum 15 GHz VLBA luminosity greater than 8×10^{26} W Hz^{-1}. The BL Lac objects without known redshifts were also included. We selected a subsample of 48 quasars that closely matched the L-z region occupied by the BL Lac objects, such that the redshift, angular size distance, and maximum 15 GHz VLBA luminosity distributions of the two subsamples were not significantly different according to K-S tests. We verified that the core and jet luminosity distributions of the two subsamples were also statistically indistinguishable.

We find that the differences in polarization between the two optical classes are still present in these matched samples, with drops in confidence level of less than 1%, mainly as a result of the smaller sample sizes. Therefore, the differences cannot be attributed to luminosity bias. The presence of these apparent differences at both 15 and 43 GHz argues against Faraday screens being the culprit, unless the rotation measures are exceptionally high. The fact that many polarized jet regions with $m > 10\%$ are seen in both BL Lac objects and quasars suggests that this is unlikely.

Our observations therefore indicate that the magnetic field properties of BL Lac and quasar jets are intrinsically different, either as a result of internal properties, such as jet power or speed, or the external environment through which the jet is propagating. There is already evidence that BL Lac jets may be the beamed versions of low-power FR I type radio galaxies, while quasars are associated with FR II sources (Urry & Padovani 1995). Numerical simulations suggest that strong shocks form more easily in low Mach number flows (P. Hughes 2004, private communication). In this case, BL Lac jets may preferen-

tially contain strong, transverse shocks that increase the field order to a higher degree than weaker, oblique shocks that develop more frequently in the jets of quasars. Another possibility, raised by Jorstad et al. (2005), is that forward and reverse shocks may have fundamentally different polarization properties, with the latter being more prevalent in BL Lac objects.

4.4. *Connections with Gamma-Ray Properties*

During its years of operation between 1991 to 1995, the EGRET instrument on board the *Compton Gamma Ray Observatory* detected approximately 60 blazars at energies above ~30 MeV. There has been much discussion as to whether these "EGRET blazars" are intrinsically different in some respect from the general blazar population. Gamma-ray emission models involving inverse Compton scattering (e.g., Dermer et al. 1992) suggest that the gamma rays are highly relativistically beamed, perhaps much more so than the radio synchrotron emission. It has been suggested that the blazars detected by EGRET have particularly high Doppler factors (Lähteenmäki & Valtaoja 2003), and kinematic studies (Kellermann et al. 2004) have indeed shown that they have faster superluminal jet speeds. This simple picture is complicated, however, by the highly variable nature of AGNs at all wavelengths, particularly in gamma rays, where rapid, energetic flaring events have been detected in many sources. The production of large gamma-ray flares in blazars appears to be closely connected with activity in the parsec-scale jets. Lähteenmäki & Valtaoja (2003) established a connection between flare activity at gamma-ray and millimeter-wave energies, and Jorstad et al. (2001a) have reported that gamma-ray flares are often associated with the appearance of new, superluminal features in the parsec-scale jet.

The MOJAVE sample offers a new means of comparing the parsec-scale jets of EGRET and non-EGRET sources, since it is selected on the basis of compact radio flux density and is not biased with respect to gamma-ray flux. It contains 26 AGNs considered to be high-probability EGRET identifications by Mattox et al. (2001) and Sowerds-Emmerd et al. (2003, 2004), as well as 12 probable identifications. We have divided the MOJAVE sample according to these EGRET classifications (listed in Table 1) and performed standard statistical tests on various properties to see whether they originate from the same parent population. For the purposes of our tests we have grouped the probable identifications into the EGRET blazar class.

We find that the EGRET and non-EGRET blazars have statistically indistinguishable optical magnitude and redshift distributions. There is a marginal difference in the total 15 GHz VLBA luminosity distributions (94% confidence), which increases to 99% confidence if the probable EGRET sources are counted instead as non-EGRET blazars. There is also a marginal indication (93% confidence) of a difference in the core luminosity distributions (the latter are calculated assuming a spectral index of zero for the cores). Clear differences are present in the parsec-scale jet features. In Figure 11 we show the 15 GHz luminosity distribution of all the Gaussian jet components fitted to the MOJAVE sample, subdivided according to gamma-ray classification. The median component luminosity in gamma-ray blazar jets is twice that of the non-EGRET blazars, and the K-S test gives only a 0.3% chance that the luminosities are drawn from the same parent distribution.

The jets in EGRET sources also have statistically higher fractional polarization levels, with a mean integrated jet polarization of 3.6% compared to 2.3% for non-EGRET sources. A survival analysis comparison of the jet polarization distributions (Fig. 12) indicates a difference at the 95% confidence level
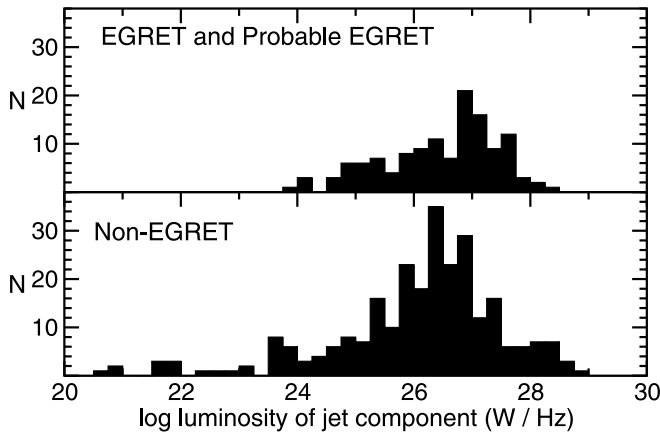
FIG. 11.—Distribution of luminosity at 15 GHz for individual jet components in gamma-ray (EGRET detected) AGNs (*top*) and non-EGRET AGNs (*bottom*) in the MOJAVE sample.
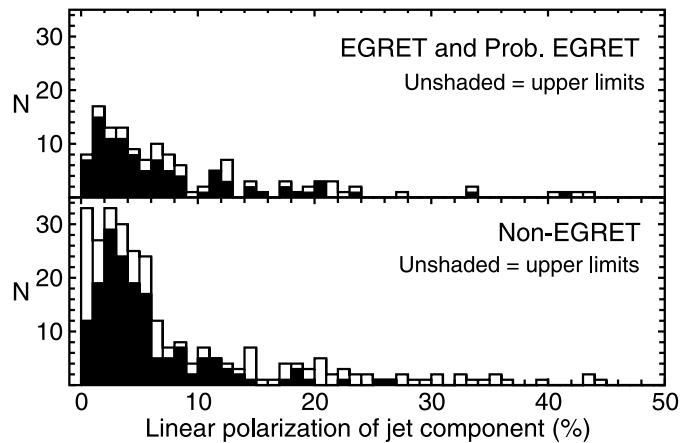

FIG. 13.—Distribution of the fractional polarization for individual components in the jets of EGRET (*top*) and non-EGRET (*bottom*) AGNs in the MOJAVE sample. The two distributions differ at the 99.9% confidence level according to a Kendall's τ test on censored data.

(99.99% if the probable EGRET sources are reclassified as non-EGRET). This is also the case for the polarization distributions of individual jet components (Fig. 13). Considering the distributions of polarization detections alone, the differences in the two classes are not large; however, the distribution of upper limits in Figure 13 indicates that the gamma-ray blazar jets are more highly polarized overall. Unlike the case of BL Lac objects versus quasars, we see no tendency for EGRET jets to be more polarized at a given distance from the core than non-EGRET jets.

These differences are perhaps unexpected, since they occur tens to hundreds of parsecs downstream of the region, where most models suggest the gamma rays are produced (near the base of the jet). It is possible that the correlated jet and gamma-ray properties of the MOJAVE blazars are not intrinsic to the jets but are instead induced by Doppler effects. EGRET blazars display a wider range of superluminal speeds (Kellermann et al. 2004), which could imply that they have higher Lorentz factors and/or jet axes aligned more closely with the line of sight. This would boost the apparent luminosity of their finite-lifetime, steep-spectrum jet features more than their non-gamma-ray counterparts. To reproduce the factor of 2 seen in the MOJAVE sample, a difference in viewing angle of only $3°$ is needed, assuming a Lorentz factor of 10 and a spectral index of -0.7. This number increases to approximately $10°$ for a Lorentz factor of 3. Such

differences in viewing angle may have a large effect on observed polarization detections, since orthogonally polarized regions may become blended via projection effects, effectively canceling their polarized signal. This would tend to lower the fractional polarizations of highly aligned jets. However, for high Lorentz factor flows, a small change in viewing angle can translate into a large change in aberrated angle in the jet rest frame, potentially *increasing* the apparent polarization of, for example, transversely shocked regions (Hughes et al. 1985). It is not clear how the observed jet electric vectors are affected in detail by viewing angle changes, since this depends largely on the mechanism that produces the polarization. If the polarization is from strong, transverse shocks, the *E*-vectors should always align with the jet flow. Unlike the case of BL Lac objects versus quasars, we find no differences in the electric vector offset distributions of the EGRET versus non-EGRET sources, which argues against intrinsic magnetic field differences.

Since the polarization differences between EGRET and non-EGRET samples are unlike those seen between BL Lac objects and quasars, more than one mechanism is probably at work. A Fisher's exact test on Table 2 shows no indication that the gamma-ray properties of MOJAVE sources are related to their optical properties (i.e., gamma-ray detections do not favor quasars over BL Lac objects). BL Lac objects show strong indications of a dramatically different magnetic field structure than quasars, perhaps as a consequence of lower jet power.

Although the Doppler factor scenario appears to account for the differences in gamma-ray blazar jet properties, it would also suggest that these should extend to the core components. We only find a marginal difference in the core luminosities of EGRET versus non-EGRET blazars and no differences in the core polarization properties. The core luminosity may depend less strongly on Doppler factor because of its flat spectral index and the fact that its emitting plasma is likely to be continuously resupplied (e.g., Lind & Blandford 1985). But as pointed out by Lister (2001), the relation may not be straightforward, since it must take into consideration inverse Compton losses, finite lifetimes of unresolved components, and possible deceleration of the flow. It is also possible that the high variability level of the cores is masking any differences in our single-epoch data set.

As a further test of our hypothesis, we have divided the component luminosities by the core luminosity in each source and applied *k*-corrections using typical spectral indices of 0 and

FIG. 12.—Distribution of the integrated fractional polarization for the jets of EGRET (*top*) and non-EGRET (*bottom*) AGNs in the MOJAVE sample.

−0.7 for the core and jet, respectively. When comparing these normalized component luminosities in which the dependence on Doppler factor has been reduced, we find no statistical differences between the EGRET and non-EGRET sources, thereby supporting our scenario.

In summary, the jet properties of gamma-ray blazars investigated here can be reconciled by assuming that they have higher Doppler factors than most blazars. This scenario can be tested more thoroughly using more complete statistics on gamma-ray blazars observed by the GLAST mission.

5. SUMMARY

We have obtained first-epoch VLBA 15 GHz linear polarization images of the first large complete AGN sample to be selected solely on the basis of compact (milliarcsecond scale) flux density. This project, entitled MOJAVE (Monitoring of Jets in Active Galactic Nuclei with VLBA Experiments), is a complement to the VLBA 2 cm Survey of Kellermann et al. (2004). Of the 133 AGNs that satisfy our selection criteria, 88% are flat-spectrum blazars having relativistic jets pointed nearly directly at us. The remainder consist of powerful, nearby radio galaxies or peaked-spectrum radio sources. The sample contains 22 weak-lined BL Lacertae objects and 38 AGNs previously detected in high-energy gamma rays by EGRET. At least 94% of the sample members have a typical one-sided core-jet morphology, which consists of a compact, bright core component located at the extreme end of a more diffuse jet. The very small number of sources with visible counterjets reflects a strong Doppler favoritism toward jets viewed end-on.

Core component properties.—The cores typically have brightness temperatures exceeding 10^{11} K, and 37% are completely unresolved, with lower limit values ranging from $\sim 10^{12}$ to 10^{14} K. The unresolved cores are more likely to show good alignments between their electric polarization vectors and the direction of the inner jet, perhaps as a result of a strong transverse shock located near the base of the jet. The cores of BL Lac objects show a particularly strong tendency toward these alignments and have higher polarization levels than the quasars. The majority of cores in the sample have fractional polarization levels below 5%, but the electric vector alignments suggest that this is not because of Faraday effects. Faraday depolarization is likely present, however, in the radio galaxy cores in our sample, none of which were detected in polarized emission.

Jet properties.—We confirm the earlier findings of Lister (2001) that the jets of BL Lac objects are more polarized than quasars at a given distance from the core. We also find that the trend of increasing fractional polarization with distance down the jet in blazars found by Lister (2001) extends to projected distances of at least 100 pc downstream. This increase in magnetic field order is not accompanied by an increase in electric

vector alignment as found at 43 GHz by Lister & Smith (2000), although we note that our observations have 3 times poorer spatial region and probe regions much farther downstream. We find many jet regions to have extremely high fractional polarization (>50%), which indicates highly ordered magnetic fields in optically thin plasma. The electric vectors of the polarized regions are more aligned with the jet ridge line in the case of BL Lac objects, consistent with strong, transverse shocks. The electric vectors in quasar jets have a variety of orientations, however, indicating either a different polarization mechanism or a tendency toward oblique shocks.

Our results imply that the magnetic field properties of parsec-scale jets are closely tied to the strength of the broad-line region in blazars. BL Lac objects have been postulated to be the end-on versions of lower power FR I type radio galaxies (Urry & Padovani 1995), and in such jets shocks may form more easily, leading to different polarization structures than those found in high-power quasars.

Gamma-ray blazars.—We have examined the properties of the 35 blazars in MOJAVE that are likely radio identifications for EGRET gamma-ray sources. The jet features in these sources are typically twice as luminous as those in non-EGRET sources and are more likely to be linearly polarized. Since these differences occur tens to hundreds of parsecs downstream of where the gamma rays are thought to be produced, the most likely explanation is that gamma-ray AGNs have slightly higher Doppler factors than typical blazars, in agreement with the conclusions of Kellermann et al. (2004).

REFERENCES

Aller, M. F., Aller, H. D., & Hughes, P. A. 2003, ApJ, 586, 33
Aloy, M., Martí, J., Gómez, J., Agudo, I., Müller, E., & Ibáñez, J. 2003, ApJ, 585, L109
Bennett, C. L., et al. 2003, ApJS, 148, 97
Best, P. N., Peacock, J. A., Brookes, M. H., Dowsett, R. E., Röttgering, H. J. A., Dunlop, J. S., & Lehnert, M. D. 2003, MNRAS, 346, 1021
Browne, I. W. A., et al. 2003, MNRAS, 341, 13
Cawthorne, T. V., & Cobb, W. K. 1990, ApJ, 350, 536
Cawthorne, T. V., & Wardle, J. F. C. 1988, ApJ, 332, 696
Cawthorne, T. V., Wardle, J. F. C., Roberts, D. H., & Gabuzda, D. C. 1993, ApJ, 416, 519
Cohen, M. H., et al. 1977, Nature, 268, 405
Dallacasa, D., Stanghellini, C., Centonza, M., & Fanti, R. 2000, A&A, 363, 887
Dermer, C. D., Schlickeiser, R., & Mastichiadis, A. 1992, A&A, 256, L27

Drinkwater, M. J., et al. 1997, MNRAS, 284, 85
Gomez, J.-L., Marscher, A. P., Alberdi, A., Jorstad, S. G., & Agudo, I. 2002, VLBA Scientific Memo 30 (Socorro: NRAO), http://www.vlba.nrao.edu/memos/sci/
Homan, D. C., Ojha, R., Wardle, J. F. C., Roberts, D. H., Aller, M. F., Aller, H. D., & Hughes, P. A. 2002, ApJ, 568, 99
Hughes, P. A. 2005, ApJ, 621, 635
Hughes, P. A., Aller, H. D., & Aller, M. F. 1985, ApJ, 298, 301
Hughes, P. A., Miller, M. A., & Duncan, G. C. 2002, ApJ, 572, 713
Jackson, C. A., Wall, J. V., Shaver, P. A., Kellermann, K. I., Hook, I. M., & Hawkins, M. R. S. 2002, A&A, 386, 97
Jorstad, S. G., Marscher, A. P., Mattox, J. R., Aller, M. F., Aller, H. D., Wehrle, A. E., & Bloom, S. D. 2001a, ApJ, 556, 738
Jorstad, S. G., Marscher, A. P., Mattox, J. R., Wehrle, A. E., Bloom, S. D., & Yurchenko, A. V. 2001b, ApJS, 134, 181

Jorstad, S. G., et al. 2005, AJ, 130, 1418
Kellermann, K. I., Vermeulen, R. C., Zensus, J. A., & Cohen, M. H. 1998, AJ, 115, 1295
Kellermann, K. I., et al. 2004, ApJ, 609, 539
Koide, S., Shibata, K., Kudoh, T., & Meier, D. L. 2002, Science, 295, 1688
Kovalev, Y. Y., Kovalev, Y. A., Nizhelsky, N. A., & Bogdantsov, A. B. 2002, Publ. Astron. Soc. Australia, 19, 83
Kovalev, Y. Y., et al. 2005, AJ, in press (astro-ph/0505536)
Kühr, H., Witzel, A., Pauliny-Toth, I. I. K., & Nauber, U. 1981, A&AS, 45, 367
Lähteenmäki, A., & Valtaoja, E. 2003, ApJ, 590, 95
Landt, H., Padovani, P., Perlman, E. S., & Giommi, P. 2004, MNRAS, 351, 83
Lavalley, M., Isobe, T., & Feigelson, E. 1992, in ASP Conf. Ser. 25, Astronomical Data Analysis Software and Systems I, ed. D. M. Worrall, C. Biemesderfer, & J. Barnes (ASP: San Francisco), 245
Lind, K. R., & Blandford, R. D. 1985, ApJ, 295, 358
Lister, M. L. 2001, ApJ, 562, 208
Lister, M. L., & Marscher, A. P. 1997, ApJ, 476, 572
Lister, M. L., Marscher, A. P., & Gear, W. K. 1998, ApJ, 504, 702
Lister, M. L., & Smith, P. S. 2000, ApJ, 541, 66
Lister, M. L., Tingay, S. J., & Preston, R. A. 2001, ApJ, 554, 964
Lobanov, A. P. 1998, A&A, 330, 79
Mattox, J. R., Hartman, R. C., & Reimer, O. 2001, ApJS, 135, 155
Middelberg, E. 2004, Ph.D. thesis, Univ. Bonn

Moellenbrock, G. A., et al. 1996, AJ, 111, 2174
Ochsenbein, F., Bauer, P., & Marcout, J. 2000, A&AS, 143, 23
Pearson, T. J., Shepherd, M. C., Taylor, G. B., & Myers, S. T. 1994, BAAS, 26, 1318
Perlman, E. S., Stocke, J. T., Carilli, C. L., Sugiho, M., Tashiro, M., Madejski, G., Wang, Q. D., & Conway, J. 2002, AJ, 124, 2401
Sowards-Emmerd, D., Romani, R. W., & Michelson, P. F. 2003, ApJ, 590, 109
Sowards-Emmerd, D., Romani, R. W., Michelson, P. F., & Ulvestad, J. S. 2004, ApJ, 609, 564
Stanghellini, C., O'Dea, C. P., Dallacasa, D., Baum, S. A., Fanti, R., & Fanti, C. 1998, A&AS, 131, 303
Stickel, M., Meisenheimer, K., & Kühr, H. 1994, A&AS, 105, 211
Taylor, G. B., Vermeulen, R. C., Readhead, A. C. S., Pearson, T. J., Henstock, D. R., & Wilkinson, P. N. 1996, ApJS, 107, 37
Teräsranta, H., Urpo, S., Wiren, S., & Valtonen, M. 2001, A&A, 368, 431
Thompson, D. J., et al. 1993, ApJ, 415, L13
Urry, C. M., & Padovani, P. 1995, PASP, 107, 803
Véron-Cetty, M.-P., & Véron, P. 2003, A&A, 412, 399
Walker, R. C., Dhawan, V., Romney, J. D., Kellermann, K. I., & Vermeulen, R. C. 2000, ApJ, 530, 233
Zavala, R. T., & Taylor, G. B. 2004, ApJ, 612, 749
Zensus, A., Ros, E., Kellermann, K. I., Cohen, M. H., Vermeulen, R. C. 2002, AJ, 124, 662